THE JOURNAL OF CHEMICAL PHYSICS **124**, 224324 (2006)

Photoionization and photodissociation of HCl($B\,^1\Sigma^+, J=0$) near 236 and 239 nm using three-dimensional ion imaging

A. I. Chichinin
Institut für Physikalische und Theoretische Chemie, Technische Universität Braunschweig, 38106 Braunschweig, Germany and Institute of Chemical Kinetics and Combustion, 630090 Novosibirsk, Russia

C. Maul[a] and K.-H. Gericke
Institut für Physikalische und Theoretische Chemie, Technische Universität Braunschweig, 38106 Braunschweig, Germany

(Received 9 February 2006; accepted 29 March 2006; published online 14 June 2006)

The electronically excited states $\mathrm{HCl}^*(E, v'=0, J'=0)$ and $\mathrm{HCl}^*(V, v'=12, J'=0)$ have been prepared by two-photon resonant absorption of ground state HCl via $Q(0)$ transitions at 238.719 and at 236.000 nm, respectively. The consequent one-or two-photon excitation at the same wavelength results in the production of H^+, Cl^+, and HCl^+ ions. The speed distributions and anisotropy parameters β for these ions have been determined by three-dimensional photofragment ion imaging based on a position-sensitive delay-line anode assembly. Several results are presented: first, we measured velocity (speed and angle) distributions for HCl^+ due to the electron recoil in the photoionization of HCl^*. Such distributions give information on the photoionization process and on the vibrational distribution of HCl^+ after the laser pulse. Second, the measured β parameters for Cl^+ and H^+ distributions give information on the symmetries of the upper states in the one-photon photoexcitation of HCl^*. Third, the measured speed distributions for H^+ help to understand the mechanism of the photodissociation of HCl^+ ions. © *2006 American Institute of Physics*.
[DOI: 10.1063/1.2198831]

I. INTRODUCTION

HCl is one of the most studied molecules in the field of reaction dynamics. It is detected by a variety of spectroscopic techniques, including photoelectron spectroscopy[1–8] (PES) and resonance enhanced multiphoton ionization (REMPI),[9–23] with both high sensitivity and high resolution. Nevertheless, even the nature of the second electronically excited state $B\,^1\Sigma^+$ was understood only recently.[10–12,17,18,24,25] In the last decade it was proven that configuration mixing of the Rydberg $E\,^1\Sigma^+$ state with the valence $V\,^1\Sigma^+$ state produces a state $B\,^1\Sigma^+$ having two minima. Because of its complicated nature, this state exhibits nontrivial rotational,[16] vibrational,[13–15,17,18] and electron[12,26,27] spectroscopies.

In the present work we report an extensive study of REMPI of HCl near 236 and 239 nm. All ions, i.e., H^+, Cl^+, and HCl^+, have been monitored. Thus, this technique is called "mass-resolved REMPI."[11] The significant production of ionized atoms in this process was originally reported by Spiglanin *et al.*,[11] and later by de Beer *et al.*,[12] Green *et al.*,[13–15] and Loock and co-workers,[26,27] who have studied this system using both REMPI and PES. The first step of the REMPI process is the resonant two-photon absorption,[9–18]

$$\mathrm{HCl}(X\,^1\Sigma^+, v'', J'') + 2h\nu \rightarrow \mathrm{HCl}^*(B\,^1\Sigma^+, v', J'), \qquad (1)$$

which produces electronically excited HCl^*. The absorption of the next photon results in different processes. It may be direct ionization or autoionization of HCl^*,

$$\mathrm{HCl}^*(B\,^1\Sigma^+, v') + h\nu \rightarrow \mathrm{HCl}^+(X\,^2\Pi_\Omega, v^+) + e^-, \qquad (2)$$

which produces vibrationally excited HCl^+ ions.[12–15,26,27] The absorption of the fourth photon leads to the photodissociation of HCl^+ ions,

$$\mathrm{HCl}^+(X\,^2\Pi_\Omega, v^+) + h\nu \rightarrow \mathrm{H}^+ + \mathrm{Cl}(^2P) \qquad (3)$$

$$\rightarrow \mathrm{H}(^2S) + \mathrm{Cl}^+. \qquad (4)$$

The H^+ ions produced in this process have been observed just recently by Loock and co-workers.[26,27]

However, ionization (2) of HCl^* is always accompanied by a one-photon transition to superexcited states HCl^{**} above their dissociation limit. These superexcited states decay into two neutral atoms, $\mathrm{H}^*+\mathrm{Cl}$ or $\mathrm{Cl}^*+\mathrm{H}$, where H^* and Cl^* denote electronically excited atoms.[12–15,26,27] Hereafter H^* and Cl^* have the meaning outlined in Table I. In the table the quartet states for $\mathrm{Cl}^*(4s)$ and $\mathrm{Cl}^*(4p)$ were omitted because they have not experimentally been observed. Quartet states do play a role for $\mathrm{Cl}^*(3d)$, where the doublet states are too high in energy to be accessed by the wavelengths employed in our study. The absorption of the fourth photon by the excited atoms results in the production of the H^+ or Cl^+ ions as follows:

---

[a] Electronic mail: c.maul@tu-braunschweig.de

TABLE I. Brief notations for excited atoms Cl^* and H^*.

Notation	Configuration	Terms
Cl^* $(4s)$	$3s^2\,3p^4[^3P]4s$	$^2P_{1/2,3/2}$
Cl^* $(4p)$	$3s^2\,3p^4[^3P]4p$	$^2D^o_{3/2,5/2},\,^2P^o_{1/2,3/2},\,^2S^o_{1/2}$
Cl^* $(4s')$	$3s^2\,3p^4[^1D]4s$	$^2D_{3/2,5/2}$
Cl^* $(3d)$	$3s^2\,3p^4[^3P]3d$	$^4D_{3/2-7/2}$
Cl^* $(3d')$	$3s^2\,3p^4[^3P]3d$	$^4F_{5/2-9/2},\,^2D_{3/2,5/2},\,^4P_{1/2-5/2},\,^2F_{5/2,7/2}$
Cl^* $(3d'')$	$3s^2\,3p^4[^3P]3d$	$^2P_{1/2,3/2}$
H^* $(n=2)$	$2s$	$^2S_{1/2}$
	$2p$	$^2P_{1/2,3/2}$

$$HCl^*(B\ ^1\Sigma^+) \xrightarrow{+h\nu} HCl^{**}$$

$$\rightarrow Cl + H^* \xrightarrow{+h\nu} Cl + H^+ + e^- \tag{5}$$

$$\rightarrow H + Cl^* \xrightarrow{+h\nu} Cl^+ + H + e^-. \tag{6}$$

This mechanism was supported by the observation of photoelectrons from the ionization of Cl^* and H^* atoms, and by the analysis of the speed distributions of Cl^+ and H^+ ions.[12–15,26,27]

Hereafter we introduce a useful notation: while the HCl^+ ions are produced in processes (1) and (2) by REMPI $(2+1_i)$, in processes (1)–(4) the H^+ and Cl^+ ions are produced by REMPI $(2+1_i+1)$, where the index i is added to label the ionizing photon. According to this notation, the formation of the atomic ions via the superexcited states in processes (1), (2), (5), and (6) is due to REMPI $(2+1+1_i)$.

In the present paper we also report, in a continuation of our recent study on photoionization of NO,[28] a new system, in which we obtain the velocity distribution of the photoions due to electron recoil in photoionization. To the best of our knowledge, there exist only three experimental studies, in which the recoil energy and angular distribution of heavy (not hydrogen) ions are determined. The first one is the study of Wolf and Helm, in which ^{87}Rb atoms, cooled in a magneto-optical trap, were two-photon ionized by a pulsed laser at 790 nm;[29,30] the second was the study of Parker *et al.* in which the recoil effects were illustrated for REMPI of D atoms cooled in a supersonic discharge expansion and also for photodissociation of HI;[31] and the third was our study of NO ionization at 226 nm.[28]

In summary, our work extends and complements the study of de Beer *et al.*[12] and Loock and co-workers.[26,27] The subject of our work is related to several areas: the first is the dynamics of the photodissociation processes of HCl^* via superexcited states [(5) and (6)], the second is ionization (2) of HCl^*, the third is photodissociation of HCl^+ ions, and, finally, we present new applications of our photofragment three-dimensional (3D) imaging technique.[32,33]

II. EXPERIMENT

The apparatus and techniques used were similar to those described previously,[32–36] and, hence, only a brief summary, emphasizing the modifications, will be given here. The experimental setup consists of a home-built single-field time-of-flight (TOF) mass spectrometer, cold supersonic molecular beam, a position sensitive detector for ions, and an optic system based on a Nd:YAG (yttrium aluminum garnet) laser-pumped dye laser. In other words, we use a photofragment imaging technique in a single-laser configuration with a special position sensitive detector named delay-line detector (DLD). The technical realization of a delay-line detector has for the first time been described in detail in Refs. 37 and 38. The detector in our apparatus was developed by Jagutzki *et al.*[39] We used a similar electronic readout circuit as described in Ref. 40. The space resolution [one ion's full width at half maximum (FWHM)] of our detector is 0.4 mm and the time resolution is about 0.5 ns. The detector $(8\times8$ cm) was introduced into the spectrometer chamber right behind the double stage microchannel plates. The transverse velocity components (v_x, v_y) of the initial velocity of each ion are determined from the measured two-dimensional impact position on the detector surface, while the measured time of arrival gives the longitudinal component (v_z) of the velocity. Hereafter the laboratory axes X, Y, and Z are directed along the laser beam, the molecular beam, and the accelerating electric field, respectively; they are mutually orthogonal. The electric vector of linear polarized laser radiation is denoted by $\boldsymbol{E}$, it is directed either along Z $(\boldsymbol{E}\|\boldsymbol{Z})$ or along Y $(\boldsymbol{E}\perp\boldsymbol{Z})$. It is worth noting that even in the cases where only TOF profiles were used in numerical analysis, the space distribution of ions was used to distinguish between the ions produced in the molecular beam and the background ions.

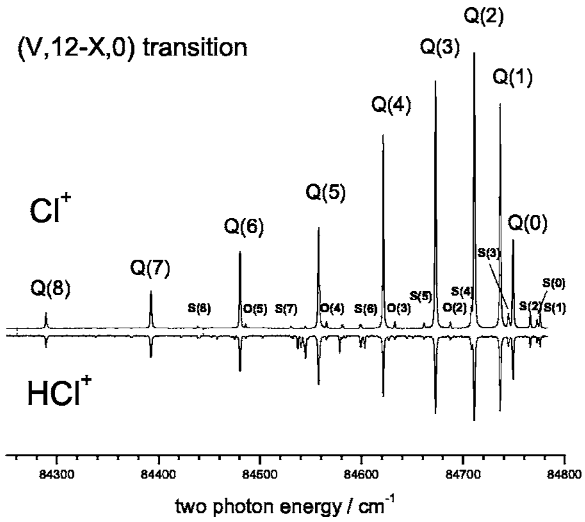

FIG. 1. REMPI detection of Cl^+ and HCl^+: Rotationally resolved and isotopically pure spectra at $T=300$ K of the transition $X(^1\Sigma^+, v''=0)\rightarrow V(^1\Sigma^+, v'=12)$.

The dye laser (Lambda Physik, Scanmate) was operated with Coumarin-47 at a repetition rate of 100 Hz, its light was frequency-doubled by a beta barium borate (BBO) crystal, separated by a Pellin-Broca prism and focused by a 20 cm lens into the ionization chamber of the TOF mass spectrometer. The laser energy was kept low to obtain approximately one event per ten laser pulses to avoid kinetic energy transfer to the fragments due to space-charge effects and to avoid saturation of the dissociation steps. The polarization of the laser was changed by a half-wave plate. Signals of the delay-

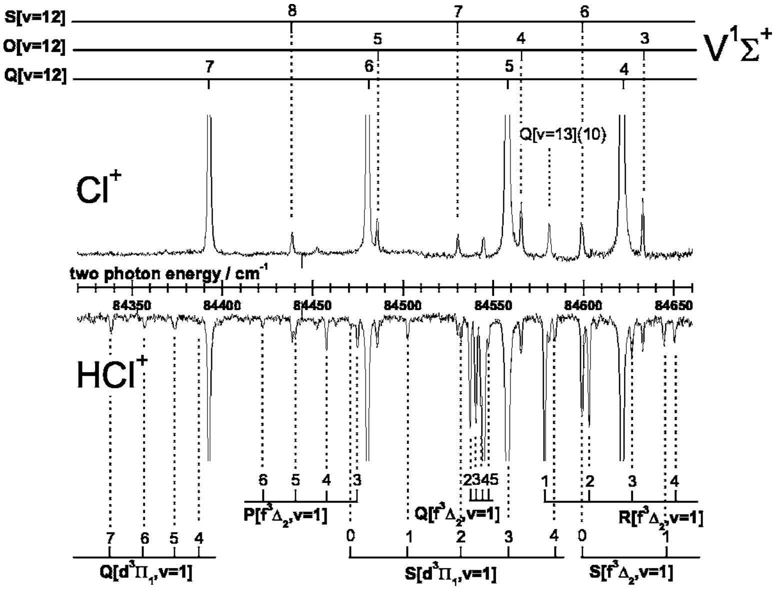

FIG. 2. Enlarged portion of the $X(^1\Sigma^+, v''=0) \rightarrow V(^1\Sigma^+, v'=12)$ transition from Fig. 1.

line detector were digitized by time-to-digital converters, accumulated over 100–200 thousand laser shots, and saved online by a personal computer.

Complementary experiments were performed on bulk HCl at 300 K in a simplified setup without 3D imaging. Here, rotationally resolved spectra were monitored for excitation into the states $E\ ^1\Sigma^+(v=0)$ and $V\ ^1\Sigma^+(v=11,12)$.

The REMPI spectrum of HCl was first reported by Arepalli *et al.*[9] More detailed studies were presented later.[10,13–15,17,18] The assignment of rotational lines of this transition was done in the work of Green *et al.*[13–15,17] Two transitions were used in the present study:

$$\mathrm{HCl}(X\ ^1\Sigma^+, v''=0, J''=0) + 2h\nu \rightarrow \mathrm{HCl}^*(E\ ^1\Sigma^+, v'=0, J'=0), \tag{1a}$$

$$\mathrm{HCl}(X\ ^1\Sigma^+, v''=0, J''=0) + 2h\nu \rightarrow \mathrm{HCl}^*(V\ ^1\Sigma^+, v'=12, J'=0). \tag{1b}$$

We denote these transitions briefly $(E,0-X,0)$ and $(V,12-X,0)$. According to Kvaran *et al.*,[18] the frequencies of these transitions are 83 780.6 cm^{-1} (238.719 nm) and 84 745.6 cm^{-1} (236.000 nm), respectively. In order to simplify the understanding of the dissociation dynamics and to avoid interference from possible alignment of the intermediate HCl* state, we analyzed only $Q(0)$ transitions which prepare the HCl* molecule in an isotropic rotational state with $J'=0$.

In order to determine the temperature of HCl in the molecular beam, we observed the first three rotational transitions $Q(0)$, $Q(1)$, and $Q(2)$ in the $(V,12-X,0)$ band where the ratio of signal intensities of $Q(0)/Q(1) \approx 3.5$. From these intensities one can estimate the HCl rotational temperature in the cold HCl/He molecular beam to be 13 K, in agreement with our previous measurements.[32]

III. VELOCITY DISTRIBUTIONS

A. REMPI detection of Cl⁺ and HCl⁺: Rotational spectra at *T*=300 K

There was only one kind of experiment in which we have detected the REMPI spectra without molecular beam at room temperature conditions. The rotationally resolved and isotopically pure spectrum of the transition $X(^1\Sigma^+, v''=0) \rightarrow V(^1\Sigma^+, v'=12)$ is shown in Fig. 1. For each transition two traces are shown: one obtained at mass 36, monitoring the HCl$^+$ ion itself, and one obtained at mass 35, monitoring the ionized chlorine Cl$^+$. Clearly and as expected, both transitions essentially consist of a strong Q branch, accompanied by weak O and S branches, while P and R branches are absent. The ratio of fragmentation with respect to ionization is significantly different for the two transitions. For excitation into $V(^1\Sigma^+, v'=12)$ fragmentation dominates over ionization. The opposite is true for excitation into $E(^1\Sigma^+, v'=0)$.

Figure 2 shows an enlarged portion of the $X(^1\Sigma^+, v''=0) \rightarrow V(^1\Sigma^+, v'=12)$ transition, where weak excitations of the $d(^3\Pi_1, v'=1)$ and $f(^3\Delta_2, v'=1)$ occur. For the latter, P and R branches are also observed. In full agreement with the work of Green *et al.*,[13] it was observed that excitation into the triplet states does not lead to fragmentation, but is exclusively followed by ionization. While not shown here, this is also true for fragmentation into H$^+$. These facts are key issues for the interpretation of the velocity distributions discussed below.

B. Distributions of HCl⁺ ions

HCl$^+$ ions are obtained by $(2+1_i)$ REMPI via ionization of HCl* in process (2). Due to the extremely low speed of the HCl$^+$ ions acquired in the ionization process, the electron recoil induced flight distance in the X, Y plane is only 500 μm, which is of the order of the spatial resolution of the DLD.[32] Therefore, only the one-dimensional projection onto the Z axis could be analyzed as shown in Fig. 3, where

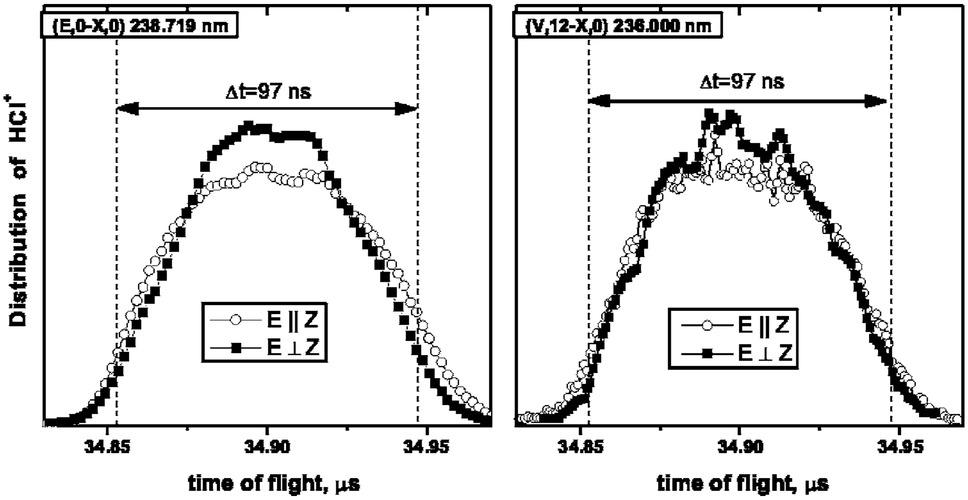

FIG. 3. TOF profiles of HCl^+ ions observed by $(2+1_i)$ REMPI of HCl for both parallel and perpendicular laser polarizations and for both $(E,0-X,0)$ and $(V,12-X,0)$ transitions. The time window Δt corresponds to the maximum possible speed of HCl^+ obtained from electron recoil in the ionization step (2). The electric field is 1.2 V/cm, the TOF is 35 μs, and the signal was accumulated over ~16 000 ions for each polarization.

typical TOF profiles of HCl^+ ions for both laser frequencies are presented. The structure of the TOF profiles of HCl^+ is determined by the electron recoil during the ionization and by the vibrational distribution of HCl^+ ions.

The maximum possible speed $v_{\max}$ of HCl^+ ions corresponds to rotationally, vibrationally, and spin-orbitally nonexcited $HCl^+(X\,^2\Pi_{3/2}, v^+=0, J^+=3/2)$ ions. The speed is calculated according to

$$v_{\max} = m_e/m_{\mathrm{HCl}}\sqrt{2(3h\nu - I_{\mathrm{HCl}})/m_e}, \tag{7}$$

where m_e and m_{HCl} are the masses of the electron and the HCl molecule, respectively, $h\nu$ is the photon energy, and I_{HCl} is the first ionization potential of HCl (12.7459 eV).[41] The values of $v_{\max}$ are found to be 15.2 and 15.7 m/s for $(E,0-X,0)$ and $(V,12-X,0)$, respectively.

The TOF window for HCl^+ ions is given by Δt

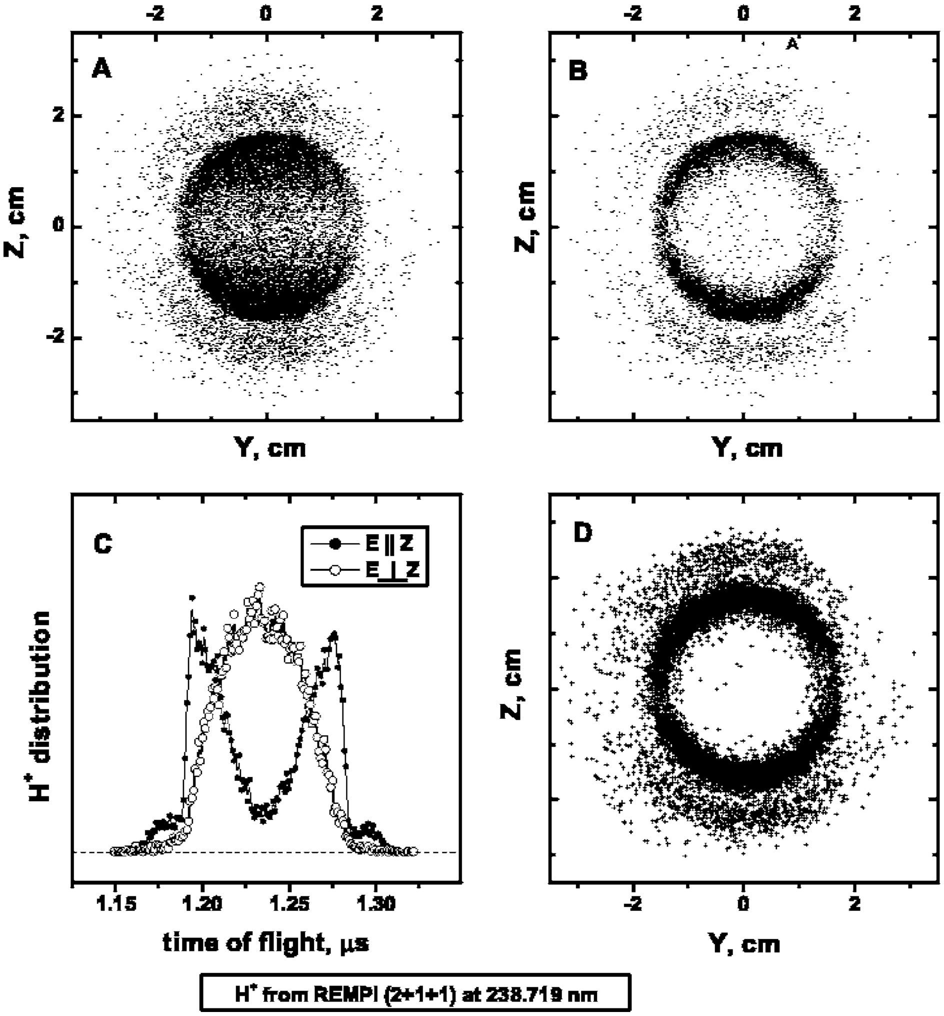

FIG. 4. Typical distributions of H^+ ions in the (2+1+1) REMPI of HCl at $(E,0-X,0)$ transition at 238.719 nm. The electric field is 30 V/cm. The polarization vector E is vertical, $E\|Z$; about 20 000 ions are shown on each picture. (A) 2D projection of the raw 3D distribution; (B) equatorial slice of a 3D image distribution; (C) TOF profiles for both laser polarizations; and (D) our projection of the raw 3D distribution, see text.

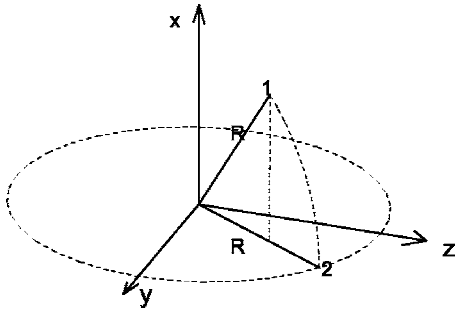

FIG. 5. The point in 3D space is labeled by number 1, the final position of the point in the *YZ* plane after our projection according to [Fig. 4(d)] is labeled by number 2. The distance *R* from the coordinate center to the point is kept constant. For comparison, the vertical projection of the point from 3D space onto the *YZ* plane according to [Fig. 4(a)] is shown by a dashed vertical line.

$=2v_{\max}/a$, where a is the acceleration due to a constant external electric field E_{ex}, $a=eE_{\text{ex}}/m_{\text{HCl}}$. The time Δt has a very simple meaning: the ions with the initial speeds $v_{\max}$ and $-v_{\max}$ along the Z axis have TOFs of $t_0-\Delta t/2$ and $t_0+\Delta t/2$, respectively. The Δt time window is also shown in Fig. 3.

One can see from Fig. 3 that the experimental TOF profiles have no sharp corners and they spread outside the Δt time window. About 4% of the ions are observed outside the theoretical TOF window. Hence additional broadening mechanisms must be taken into account. A broadening due to an inhomogeneity of the electric field may be excluded since different parts of the two-dimensional image of the molecular beam yield identical TOF distributions. The duration of the laser pulse introduces a broadening of the TOF distribution by 3–5 ns, which is not sufficient either to explain the observed broadening. Thus we assume that the observed broadening is due to the interaction between HCl^+ ions and the electric field, created by ions collected on the insulating electrode mounts inside the spectrometer chamber. This assumption is based on the fact that the TOF of HCl^+ ions increases slightly during a measurement.

The speed distributions of HCl^+ ions were obtained from TOF profiles by both a forward convolution analysis in which the apparatus function was taken into account[42] and by the procedure described in the Appendix. For typical profiles with an average TOF of 35 μs, the apparatus function was expected to be a Gaussian with a FWHM width of 30 ns.

C. Distributions of H^+ ions

1. Methods of 2D visualization of 3D data

The analysis of the observed raw 3D data of H^+ ions is always performed fully three-dimensionally. Hence, information about all three spatial coordinates directly result from experimental measurement rather than from mathematical reconstruction, as is common and unevitable in 2D imaging experiments.[43]

However, whereas a fully three-dimensional analysis of 3D data can be performed, a conventional 2D presentation of 3D data requires projection. We feel that an informative 2D presentation of a raw 3D distribution is really a challenging task. The presentation of the raw experimental data should be straightforward, with minimal mathematical manipulation.

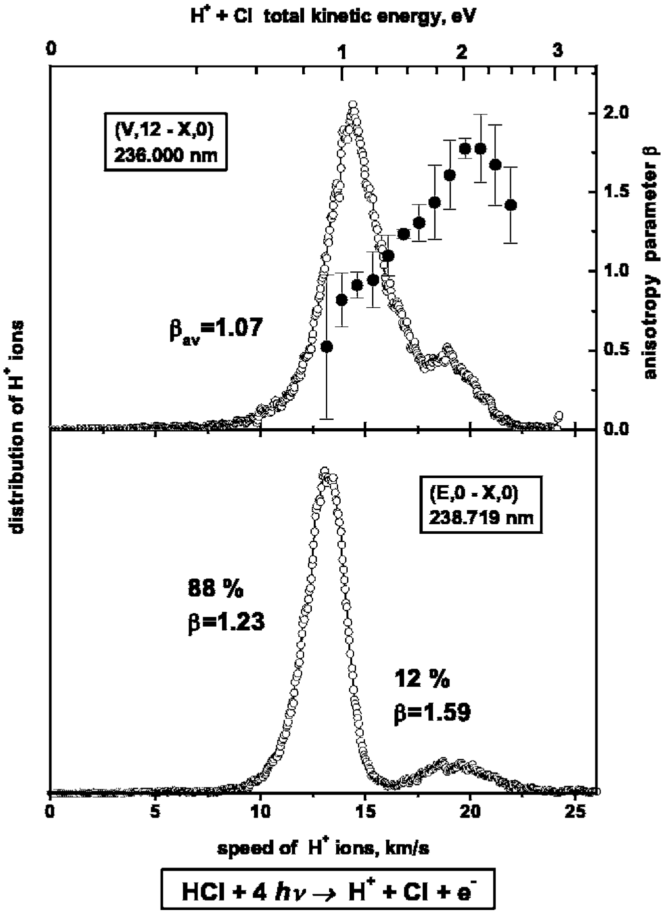

FIG. 6. Speed distributions of H^+ ions in $(2+1_i+1)$ REMPI (fast ions) and $(2+1+1_i)$ REMPI (slow ions) of HCl. For the $(V,12-X,0)$ transition (top panel) the anisotropy parameter β as a function of speed is presented as black circles, with the scale shown on the right vertical axis. For the $(E,0-X,0)$ transition (bottom panel) individual β parameters for each peak are presented.

For illustrative purposes in Fig. 4 we present the H^+ ion data in different manners. One of them is a 2D projection of the raw 3D data [Fig. 4(a)], another is an equatorial slice of a 3D distribution [Fig. 4(b)], which has a width of 1.5 cm. The disadvantage of such a slice presentation is the loss of the main part of the data, since the slice must be rather narrow to be meaningful.

To be informative, the plane of the slice must contain the electric vector $\boldsymbol{E}$. It is interesting to note that there are two possibilities to generate an informative slice. The first one (YZ) is perpendicular to the laser beam directed along the X axis, and the second one is either XZ, if $\boldsymbol{E}\|\boldsymbol{Z}$, or XY, if $\boldsymbol{E}\|\boldsymbol{Y}$. Note that we have found the quality of the (YZ) slice to be slightly better than the quality of the second one because the length of the laser spot and the background ions contribute to the signal mainly along the X axis. However, this may not be the only reason for the observed effect.

Another reason for differing projections could be proton flyout, in particular, if the time of ionization of $H^*(n=2)$ is larger than ca. 1 ns. Since the observed differences are small, we conclude that the ionization of $H^*(n=2)$ is fast.

The third presentation of a 3D velocity distribution is a one-dimensional projection onto the Z axis, which is typical for TOF mass spectrometry [TOF profiles, Fig. 4(c)].

TABLE II. Summary of total kinetic energy distributions (experimental and theoretical) and β parameters.

Ion	Transition	E_{exp} (eV)[a]	E_{calc} (eV)	β	Fraction	Source
H^+	$(E,0\text{-}X,0)$	0.93	0.92[b,c]	1.23 ± 0.1	0.88	H^*
		1.4–2.8	⋯	1.59 ± 0.2	0.12	HCl^+
	$(V,12-X,0)$	1.11	1.08[b,c]	0.9 ± 0.2	0.77[d]	H^*
		1.3–2.8	⋯	1.6 ± 0.2	0.23[d]	HCl^+
Cl^+	$(E,0-X,0)$	0.56	0.58–0.65[b,e]	1.4 ± 0.4	0.77	Cl^* $(4s'/4p)$
		1.6–2.2	1.95[b,f]	1.9 ± 0.2	0.23	Cl^* $(4s)$
	$(V,12-X,0)$	0.02	0.03[g]	1.48 ± 0.2[h]	0.06	Cl^* $(3d')$
		0.13	0.15[i]	1.48 ± 0.2[h]	0.12	Cl^* $(3d')$
		0.69	0.76–0.83[b,e]	0.41 ± 0.4	0.61	Cl^* $(4s'/4p)$
		1.6–2.1	2.12[f]	1.6 ± 0.3	0.21	Cl^* $(4s)$
HCl^+	$(E,0-X,0)$		4.6×10^{-5}[j]	0.3 ± 0.2	1	
	$(V,12-X,0)$		4.3×10^{-5}[j]	0.2 ± 0.2	1	

[a] Our experimental results: The maxima of the energy distributions or energy ranges are presented.

[b] E_{calc} is the theoretical position of the maximum total kinetic energy, calculated by $E_{calc}=3h\nu-D(HCl)-E(A^*)$, where $E(A^*)$ is the electronic energy of excited atom before ionization.

[c] $H^++Cl(^2P_{1/2})+e$ products are assumed.

[d] The result of decomposition, see Fig. 12.

[e] For all components of Cl^* $(4p)$ between $^2S^0_{1/2}$ and $^2D^0_{5/2}$.

[f] Calculated for the dominant $Cl^*(^2P_{3/2})$ component of Cl^* $(4s)$.

[g] For $^2D_{5/2}$ components of Cl^* $(3d')$.

[h] The average β parameter for both peaks at 0.02 and 0.13 eV.

[i] For $^4F_{9/2}$ components of Cl^* $(3d')$.

[j] $E_{calc}=m_{HCl}v^2_{max}/2$ is the maximum possible kinetic energy of HCl^+, see Eq. (7).

The fourth representation [Fig. 4(d)] is our proposal on how to generate a 2D presentation of a 3D velocity distribution. The principle of this diagram is illustrated in Fig. 5, where the projection of a point in 3D space onto the YZ plane is shown. One may imagine this projection as a "fall" of a point from 3D space onto the YZ plane, conserving the distance from the coordinate center to the point. The point in 3D space, its projection onto the YZ plane, and the coordinate center are all placed in a vertical plane. After the projection a point with 3D coordinates (x,y,z) has the new coordinates $(0,y/\sqrt{1-(x/R)^2},z/\sqrt{1-(x/R)^2})$ in the YZ plane, where $R=(x^2+y^2+z^2)^{1/2}$. The advantage over the slice method B is that we show all experimental points. A disadvantage is a less intuitive quick interpretation of the angular distributions. For example, in the case of a perpendicular transition ($\beta=-1$) the probability to find the ion flying along the direction of the electric vector $\boldsymbol{E}$ is equal to zero, while it appears not to be zero in our projection. On the other hand, our picture very well presents the case of a parallel transition ($\beta=2$), in which the probability to find the ion flying perpendicular to the direction of the electric vector $\boldsymbol{E}$ is equal to zero.

This representation proved to be useful in determining the scaling parameter, which converts times of flight into space coordinates. This parameter is usually calculated theoretically and then this calculation is verified by making two such projections of the 3D distribution onto the XZ and YZ planes and comparing them. If the parameter is correct, we obtain two concentric circular rings. If not, we obtain two ellipses, one of which is elongated vertically and the other one horizontally.

2. Velocity distributions of H^+ *ions*

In Fig. 6 the speed distributions of H^+ ions observed at two different wavelengths are presented. These one-dimensional presentations are obtained from the 3D data. The total kinetic energy E_t of the H^++Cl system is shown at the upper scale, as calculated from the speed V of the H^+ ions: $E_t=(36/35)m_HV^2/2$, where m_H is the mass of H^+. From Figs. 4 and 6 it can be seen that the speed distributions consist of two peaks. In the case of the $(V,12\text{-}X,0)$ transition (top panel of Fig. 6) the peaks overlap, and hence the dependence of the anisotropy parameter β on the speed of the H^+ ion is presented. In the case of the $(E,0\text{-}X,0)$ transition (bottom panel of Fig. 6) the peaks are well separated and can be characterized by individual β parameters. The summary of energy distributions and β parameters obtained in this study is presented in Table II.

D. Distributions of Cl^+ ions

TOF profiles of Cl^+ ions at both laser frequencies contain two groups of "fast" Cl^+ ions resulting mainly from parallel transitions, see Fig. 7. The interesting difference between the TOFs for $(E,0\text{-}X,0)$ and $(V,12\text{-}X,0)$ transitions is the presence of the group of very low-energy Cl^+ ions in the latter case. These speed distributions of Cl^+ ions are obtained from the profiles by both forward convolution analysis[42] and by the procedure described in the Appendix. The X,Y space distribution was not studied because of the very low speed of the ions.

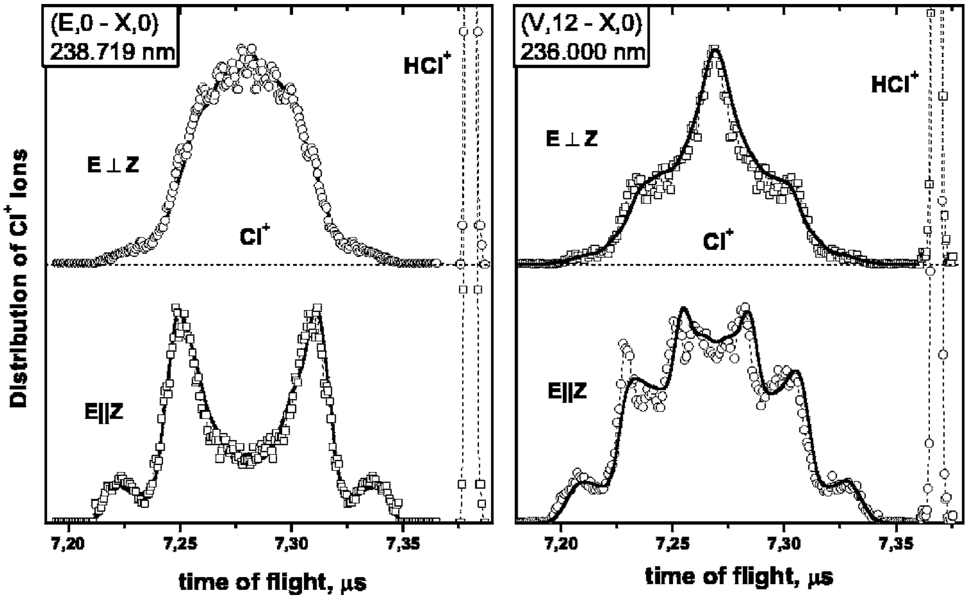

FIG. 7. Typical TOF profiles of Cl^+ ions in (2+1+1) REMPI of HCl for both laser frequencies. The solid plot shows the result of the fitting procedure. The narrow peak at the right side of each picture belongs to HCl^+. The peaks of very low energy Cl^+ ions produced by a mainly parallel transition is present at the $(V,12-X,0)$ transition (right panel) and absent at the $(E,0-X,0)$ transition (left panel).

IV. DISCUSSION

A. Correlation diagram data

The photoionization and photodissociation of state-selected $HCl^*(B\ ^1\Sigma^+, J'=0)$ is a complex process where several pathways are involved. The detailed information about all ionic products will help to elucidate all decay mechanisms. Since this wealth of information is also sometimes confusing, it might help to orient oneself in advance at the final result of pathways which are shown in Fig. 8.

The complete correlation diagram for dissociation of HCl is too complex to be shown here, instead we present the basis for the diagram in Table III. In this table, all possible states of the separated H+Cl products which may be obtained by three-photon excitation $(3h\nu \leq 15.76\text{ eV})$ of HCl are listed in the central column in order of increasing energy. The correlated bound and repulsive states of HCl are listed to the left and to the right, respectively. Spin-orbit splittings are omitted, with energies shown for the lowest spin-orbit terms. Note that all bound states have almost the same internuclear distance and vibrational frequency. The main exception is the B state, which has a double-minimum potential energy curve, being a mixture of the Rydberg $E\ ^1\Sigma^+$ and the valence $V\ ^1\Sigma^+$ states.

The correlation table is based on the terms of the HCl^+ ion calculated by Pradhan *et al.*[44] The bound states of HCl^+ are $X\ ^2\Pi$ and $A\ ^2\Sigma^+$, they correlate to $H+Cl^+(3p^4[^3P])$ and $H^+ + Cl(3p^5[^2P_J])$, respectively. All other relevant states of HCl^+ are repulsive. We obtain several sets of Rydberg states of HCl by adding one $nl\lambda$ electron to the configurations of HCl^+. Since the bound Rydberg states of HCl have $X\ ^2\Pi$ and $A\ ^2\Sigma^+$ cores, they correlate to $H+Cl^*(3p^4[^3P]nl)$ and $H^*(n'l)+Cl$, respectively; all other Rydberg states of HCl are repulsive. We also assume that the repulsive term $HCl^+ \rightarrow H+Cl^+(^1D)$ after addition of a $4s$ electron corresponds to $HCl \rightarrow H+Cl^*(3p^4[^1D]4s)$. We cannot point out the terms which lead to $H+Cl(3s\,3p^6\ ^2S[^{1,3}\Sigma^+])$ products, but this state of chlorine atom is unimportant since it involves ionization of Cl atom via two-electron transition $Cl(3s\,3p^6)+h\nu \rightarrow Cl^+(3s^2\,3p^4)+e$.

When it is possible, the experimental values of bound

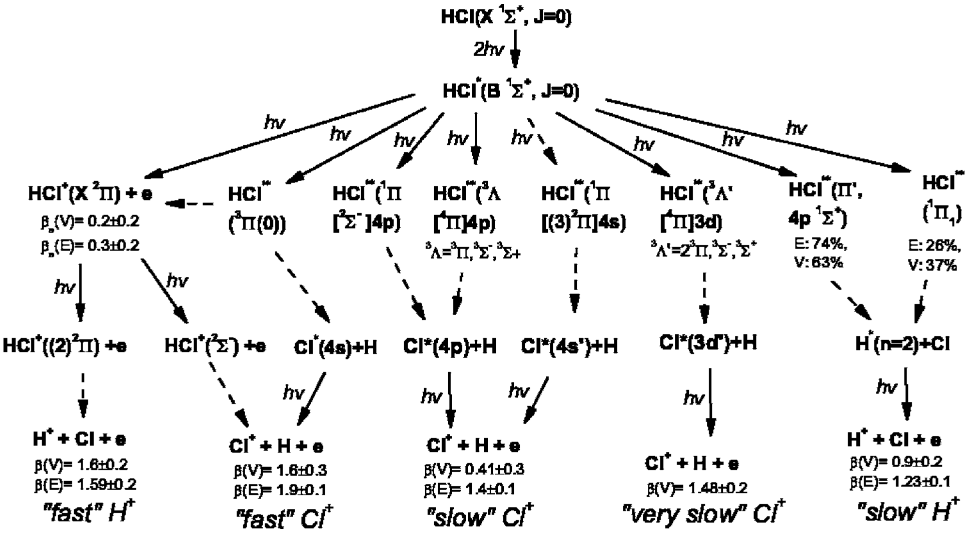

FIG. 8. The pathways which have been observed in the present study, see also Table II. The solid and dashed arrows denote photoinduced and spontaneous transitions, respectively. $\beta(V)$ and $\beta(E)$ denote β parameters for the $(V,12-X,0)$ and $(E,0-X,0)$ transitions, respectively. β_e denote β parameters for the ionization process.

states of HCl are presented; when they are unknown, theoretical values are shown. As many authors,[23,45,46] the *d* states in the range of 10.77–11.16 eV we label as 3*d*, although other authors label these states as 4*d*.[25,47] Also, we assign the states $m\,^3\Pi$, $M\,^1\Pi$, $r\,^3\Pi$ and $R\,^1\Pi$ to 5*s* and $5p\pi$ excitations,[46,48] but not to $4d\sigma$, $e\sigma$, or $f\sigma$.[23,45,47] The states $k\,^3\Pi$, $K\,^1\Pi$, $l\,^3\Phi$, and $L\,^1\Phi$ we assign to $4d\delta$ excitation, but not to $a\delta$.[45] In the table we assume that the energies of the $J\,^1\Sigma^-$ and $i\,^3\Delta$ states are very close to $H\,^1\Sigma^+$ and $I\,^1\Delta$ states, as is calculated by Bettendorff *et al.*[25]

Hereafter we denote $(\sigma,\pi^4[A\,^2\Sigma^+]nl\lambda)$ and $(\sigma^2,\pi^3[(2)^2\Pi]nl\lambda)$ configurations as $(A,nl\lambda)$ and $(\Pi',nl\lambda)$, respectively. The important repulsive term $^3\Pi(0^+)$ with configuration $\sigma,\pi^3,\sigma^*[^4\Pi]4s$ will be denoted as $^3\tilde{\Pi}_0$.

B. Potential energy curves

Selected potential energy curves for HCl and HCl$^+$ are shown in Fig. 9. All states of $^1\Sigma^+$ symmetry with energy below the energy of three photons are presented in the figure, except Rydberg states of HCl with $\sigma^2,\pi^3[^2\Pi]$ core and highly excited outer electrons $(n\geqslant 5)$. The ground state HCl(X) is a Morse curve, which coincides almost perfectly with the *ab initio* curve.[25] All curves for HCl$^+$ are taken from *ab initio* calculations of Pradhan *et al.*,[44,52] but corrected to reproduce asymptotic spectroscopic energies. The curves for bound superexcited states of HCl$^{**}(A,nl\lambda)$ are shown as Morse curves with parameters given in Table IV. The curves for bound superexcited states of HCl$^{**}(^1\Sigma^+)$ are taken from the *ab initio* study of Bettendorff *et al.*[25] We assume also that the repulsive terms $^3\tilde{\Pi}_0$, $(\Pi',4s)$, and $(\Pi',4p\pi)$ of HCl are strictly parallel to the corresponding terms of HCl$^+$.

The curve for the HCl$^*(B)$ state requires special attention. The internuclear distance r_0 for the *V* state may also be obtained from the nearly equal rotational constants B_v for low-lying $v_V'=3-7$ vibrational states.[18] For the *E* state the distance r_0 may be taken from *ab initio* calculations.[25] It is difficult to construct the potential curve, or only the barrier height between *E* and *V* states, because it is impossible to treat the *B* state as a single state, without considering nonadiabatical transitions between *E* and *V* states. For example, the $(E,1)$ state is placed much higher than the barrier, but it has an equilibrium distance r_0 almost equal to the $(E,0)$ state, and this distance r_0 is much lower than the typical r_0 values for the *V* state.

In addition, both $(E,0)$ and $(E,1)$ vibrational states are almost in resonance and interact strongly with $(V,10)$ and $(V,14)$ vibrations, respectively,[18] which is supported by the thorough deperturbation analysis of Liyanage *et al.*[53]

An important conclusion is that the vibrational wave functions of the states $(E,0)$ and $(V,12)$ are not localized in the *E* and *V* potential wells, but distributed over both wells.

In the range $r\leqslant 2.6$ Å, the energy curve for the *E* state is the *ab initio* curve,[25] which is downshifted by 0.22 eV in order to reproduce the energy of the ground vibrational state. Outside of this range the Morse curve is used. The *ab initio* calculations for the energy of the *V* state are in poor agreement with experiment probably because the state correlates to H$^+$+Cl$^-$. For example, the calculations predict the energy of the $(V,0)$ vibrational state to be 10.15 eV, while it is 9.484 eV. Hence the *V* state is constructed from two parts. The repulsive part of this state is the *ab initio* curve,[25] and at large internuclear distances, it is a Morse potential. Since the *V* state correlates to the H$^+$+Cl$^-$ ion pair, a Coulomb potential should be used for distances close to or larger than 4 Å. The curve for the H state is the *ab initio* curve[25] when $r<2.0$ Å, and for larger *r*, it is a Morse curve.

C. Lifetimes

Energies of HCl$^+(X,{}^2\Pi_\Omega,v^+)$ were determined in a photoelectron study of Yencha *et al.*[7] $(2+1_i)$ REMPI can produce only HCl$^+$ ions in the ground state $X\,^2\Pi$ with vibrational excitation up to $v^+=10$ and $v^+=11$, for $(E,0\text{-}X,0)$ and $(V,12\text{-}X,0)$, respectively. However, four-photon REMPI can produce H$^+$ and Cl$^+$ ions via the $(2+1+1_i)$ scheme by ionization of excited H$^*(n=2)$ and Cl* atoms and via the $(2+1_i+1)$ scheme by photodissociation of HCl$^+$.

While H$^*(2s)$ and Cl$^*(4p)$ states are stable on the nanosecond scale, the lifetimes of H$^*(2p)$ and Cl$^*(4s)$) are 1.6 and 2.0 ns, respectively, which is comparable to the duration of the laser pulse. Hence in the excited states H$^*(n=2)$ and Cl$^*(4s,4p)$ the population ratios $[\mathrm{H}^*(2p)]/[\mathrm{H}^*(2s)]$ and $[\mathrm{Cl}^*(4s)]/[\mathrm{Cl}^*(4p)]$ are controlled not only by the dynamics of the photodissociation processes, but also by spontaneous decay. This is an additional difficulty in comparison to signal amplitudes obtained by different probing lasers. Note, for example, that de Beer *et al.*[12] and Loock and co-workers[26,27] used a XeCl excimer pumped dye laser with a pulse width of ca. 10–15 ns, while our Nd:YAG laser-pumped dye laser has a pulse width of 3–5 ns. Hence the population ratios may be larger in our study. Note also that the average lifetime for HCl$^*(B\,^1\Sigma^+)$ is 1.6 ns.[54]

The typical radiative lifetime of vibrationally excited ions HCl$^+(^2\Pi_{1/2,3/2},v^+=1)$ is about 13.2 ± 2 ms,[55,56] much larger than the duration of the laser pulse, hence the vibrational decay of HCl$^+$ ions may be neglected. All the signals of ions occur only at the rather narrow absorption line of HCl, hence the participance of clusters may be ruled out.

Although we could not accurately determine the ratio of intensities of H$^+$, Cl$^+$, and HCl$^+$ REMPI peaks, we have found that the higher the laser energy is, the larger is the signal ratio $S(\mathrm{Cl}^+)/S(\mathrm{HCl}^+)$. This is easily understood, since HCl$^+$ is produced by three-photon REMPI $(2+1)$, while Cl$^+$ and H$^+$ are produced by four-photon REMPI $(2+1+1)$.

D. Is Cl$^+$ produced via bound or repulsive states of HCl**?

In Figs. 1 and 2 the REMPI spectral bands which correspond to transitions via the $f\,^3\Delta$ and $d\,^3\Pi$ triplet states are absent for Cl$^+$ and present for HCl$^+$, while the transitions via the *B* state are present in both cases. We explain this fact as follows.

From Table III it is clear that the $f\,^3\Delta$ and $d\,^3\Pi$ states belong to the same electronic configuration and have similar

TABLE III. The correlation data for dissociation of the HCl molecule with excitation energy below 15.76 eV.

Bound states		States at $r\rightarrow\infty$	Repulsive states	
Configuration[a]	Terms $\{E,\text{eV}\}$	Terms[b] $\{E,\text{eV}\}$	Configuration[a]	Terms
σ^2,π^4	$X\,^1\Sigma^+\{0.00\}$	H+Cl $^{1,3}[\Sigma^+,\Pi]\{4.43\}$	σ^2,π^3,σ^* σ,π^4,σ^*	$A\,^1\Pi,a\,^3\Pi$ $t\,^3\Sigma^+$
$\sigma^2,\pi^3[^2\Pi]4s$ (R_1)	$b\,^3\Pi\{9.28\}$, $C\,^1\Pi\{9.61\}$	$\mathrm{H}+\mathrm{Cl}^*(3p^4[^3P]4s)$ $^4P:{}^{3,5}[\Sigma^-,\Pi]\{13.35\}$ $^2P:{}^{1,3}[\Sigma^-,\Pi]\mathbf{\{13.64\}}$[c]	$\sigma^2,\pi^2,\sigma^*[^2\Sigma^-]4s$ $\sigma^2,\pi^2,\sigma^*[^4\Sigma^-]4s$ $\sigma,\pi^3,\sigma^*[^4\Pi]4s$	$^{1,3}\Sigma^-$ $^{3,5}\Sigma^-$ $^3\Pi(\equiv\tilde{\Pi}),{}^5\Pi$
$\sigma,\pi^4\sigma^*$	$V\,^1\Sigma^+\{9.484\}$[d]	$\mathrm{H}^++\mathrm{Cl}^-$ $[^1\Sigma^+]\{14.42\}$		
$\sigma,\pi^4[A\,^2\Sigma^+]4s$ $(R_3)(A,4s)$[f]	$^1\Sigma^+\{12.92\}$,[e] $^3\Sigma^+\{13.11\}$	$\mathrm{Cl}+\mathrm{H}^*(2s\,^2S)$ $^{1,3}[\Sigma^+,\Pi]\mathbf{\{14.63\}}$[c]	$\sigma^2,\pi^3[(2)^2\Pi]4s$ $(\Pi',4s)$[f]	$^{1,3}\Pi$
$\sigma,\pi^4[A\,^2\Sigma^+]4p\sigma$ $(A,4p\sigma)$[f] $\sigma,\pi^4[A\,^2\Sigma^+]4p\pi$ $(A,4p\pi)$[f]	$^1\Sigma^+\{13.82\}$,[e] $^3\Sigma^+$ $^1\Pi\{13.72\}$,[e] $^3\Pi$	$\mathrm{Cl}+\mathrm{H}^*(2p\,^2P)$ $^{1,3}[2\Sigma^+,\Sigma^-,2\Pi,\Delta]$ $\mathbf{\{14.63\}}$[c]	$\sigma^2,\pi^3[(2)^2\Pi]4p$ $(\Pi',4p)$[f]	$^{1,3}[\Sigma^+,\Sigma^-,$ $\Pi,\Delta]$
$\sigma^2,\pi^3[^2\Pi]4p\sigma$ (R_2) $\sigma^2,\pi^3[^2\Pi]4p\pi$ (R_1)	$d\,^3\Pi\{10.12\}$, $D\,^1\Pi\{10.23\}$ $^3\Sigma^+\{10.11\}$, $f\,^3\Delta\{10.15\}$, $E\,^1\Sigma^+\{10.255\}$,[d] $F\,^1\Delta\{10.27\}$, $G\,^1\Sigma^-\{10.32\}$, $g\,^3\Sigma^-\{10.39\}$	$\mathrm{H}+\mathrm{Cl}^*(3p^4[^3P]4p)$ $^4P:{}^{3,5}[\Sigma^+,\Pi]\{14.71\}$ $^4D:{}^{3,5}[\Sigma^-,\Pi,\Delta]\{14.83\}$ $^2D:{}^{1,3}[\Sigma^-,\Pi,\Delta]\mathbf{\{14.93\}}$[c] $^2P:{}^{1,3}[\Sigma^+,\Pi]\mathbf{\{15.00\}}$[c] $^4S:[^{3,5}\Sigma^-]\{15.06\}$ $^2S/^2P:[^{1,3}\Sigma^-]\mathbf{\{15.08\}}$[c]	$\sigma^2,\pi^2,\sigma^*[^2\Sigma^-]4p$ $\sigma^2,\pi^2,\sigma^*[^4\Sigma^-]4p$ $\sigma,\pi^3,\sigma^*[^4\Pi]4p$	$^{1,3}[\Sigma^-,\Pi]$ $^{3,5}[\Sigma^-,\Pi]$ $^{3,5}[\Sigma^+,\Sigma^-,$ $\Pi,\Delta]$
		$\mathrm{H}+\mathrm{Cl}^*(3p^4[^1D]4s\,^2D)$ $^{1,3}[\Sigma^+,\Pi,\Delta]$ $\{14.86\}$	$[(2)^2\Sigma^+]4s$[g] $\sigma,\pi^3\sigma^*[(3)^2\Pi]4s$ $\sigma^2,\pi^2,\sigma^*[^2\Delta]4s$	$^{1,3}\Sigma^+$ $^{1,3}\Pi$ $^{1,3}\Delta$
	?[h]	$\mathrm{H}+\mathrm{Cl}^*(3s.3p^6\,^2S)$[h] $[^{1,3}\Sigma^-]\{15.06\}$		
$\sigma^2,\pi^3[^2\Pi]3d\sigma$ (R_3) $\sigma^2,\pi^3[^2\Pi]3d\pi$ (R_2) $\sigma^2,\pi^3[^2\Pi]3d\delta$	$n\,^3\Pi\{10.87\}$,[i] $N\,^1\Pi\{11.16\}$[i,j] $h\,^3\Sigma^+\{10.88\}$[k] $i\,^3\Delta,I\,^1\Delta\{10.98\}$,[l] $J\,^1\Sigma^-,H\,^1\Sigma^+\{11.00\}$,[i,j] $j\,^3\Sigma^-\{11.08\}$[j] $k\,^3\Pi\{10.93\}$[i] $K\,^1\Pi\{11.12\}$,[k,j] $L\,^1\Phi\{11.16\}l\,^3\Phi$	$\mathrm{H}+\mathrm{Cl}^*(3p^4[^3P]3d)$ $^4D:{}^{3,5}[\Sigma^+,\Pi,\Delta]\mathbf{\{15.34\}}$[c] $^4F:{}^{3,5}[\Sigma^-,\Pi,\Delta,\Phi]\mathbf{\{15.61\}}$[c] $^4P:{}^{3,5}[\Sigma^-,\Pi]\mathbf{\{15.72\}}$[c] $^2F:{}^{1,3}[\Sigma^-,\Pi,\Delta,\Phi]\{15.73\}$ $^2D:{}^{1,3}[\Sigma^-,\Pi,\Delta]\{15.73\}$ $^2P:{}^{1,3}[\Sigma^-,\Pi]\{15.78\}$	$\sigma^2,\pi^2,\sigma^*[^2\Sigma^-]3d$ $\sigma^2,\pi^2,\sigma^*[^4\Sigma^-]3d$ $\sigma,\pi^3,\sigma^*[^4\Pi]3d$	$^{1,3}\Sigma^-$, $^{1,3}\Pi,{}^{1,3}\Delta$ $^{3,5}\Sigma^-$, $^{3,5}\Pi,{}^{3,5}\Delta$ $^{3,5}[\Sigma^+,\Sigma^-,$ $2\Pi,\Delta,\Phi]$
$\sigma^2,\pi^3[^2\Pi]$ $(5s,5p\sigma,5p\pi)$	$m\,^3\Pi,M\,^1\Pi,r\,^3\Pi,R\,^1\Pi$, $^{1,3}\Sigma^+,{}^{1,3}\Sigma^-,{}^{1,3}\Delta$ $\{11.13\text{–}11.70\}$[n]	$\mathrm{H}+\mathrm{Cl}^*(3p^4[^3P]5s,5p$ $^{2,4}S,{}^{2,4}P,{}^{2,4}D)$ $\{15.76\text{–}16.41\}$	$[^2\Sigma^-,{}^4\Sigma^-,{}^4\Pi](5s,5p)$	$[2\,^1\Sigma^-,{}^3\Sigma^+,5\,^3\Sigma^-,$ $^5\Sigma^+,3^5\Sigma^-,{}^1\Pi,$ $4\,^3\Pi,3\,^5\Pi,{}^{3,5}\Delta]$

[a] Molecular orbitals 5σ, 2π, and $6\sigma^*$ are denoted as σ, π, and σ^*. The configuration indices introduced by Bettendorff *et al.* (Ref. 15), are shown in round brackets.

[b] Notation: $^{n,m}[\Sigma,\Pi,\ldots]\equiv[^n\Sigma,{}^m\Sigma,{}^n\Pi,{}^m\Pi,\ldots]$ (Ref. 49).

[c] Detected in the present study.

[d] Reference 18.

[e] Reference 50.

[f] Short labels for electronic configurations.

[g] A mixture of σ^0,π^4,σ^* and σ^2,π^2,σ^* configurations.

[h] Unassigned. Chlorine atomic state is a mixture of $3s\,3p^6$ (49%) and $3s^2\,3p^4[^1D]$ (25%).

[i] Reference 45.

[j] Reference 47.

[k] Reference 25.

[l] Reference 51.

[m] Reference 23.

[n] Reference 46.

energies as the $E\,^1\Sigma^+$ state. The E state, being the Rydberg part, i.e., the inner well, of the $B\,^1\Sigma^+$ state should behave identically to the triplet Rydberg states with regard to subsequent absorption of a third photon. Thus, excitation from the Rydberg well must lead to ionization only.

The fragmentation is a unique behavior of the $B\,^1\Sigma^+$, which must be caused by the presence of the outer valence well of the potential, i.e., by the admixture of the $V\,^1\Sigma^+$ state. Obviously, the absorption of a third photon at the large internuclear distances characteristic of the valence well opens up new exit channels out of the $B\,^1\Sigma^+$ state, leading to fragmentation of HCl. Obvious candidates for target states resulting from photoexcitation of the B state at large internuclear distances are the repulsive Rydberg states, correlating to H

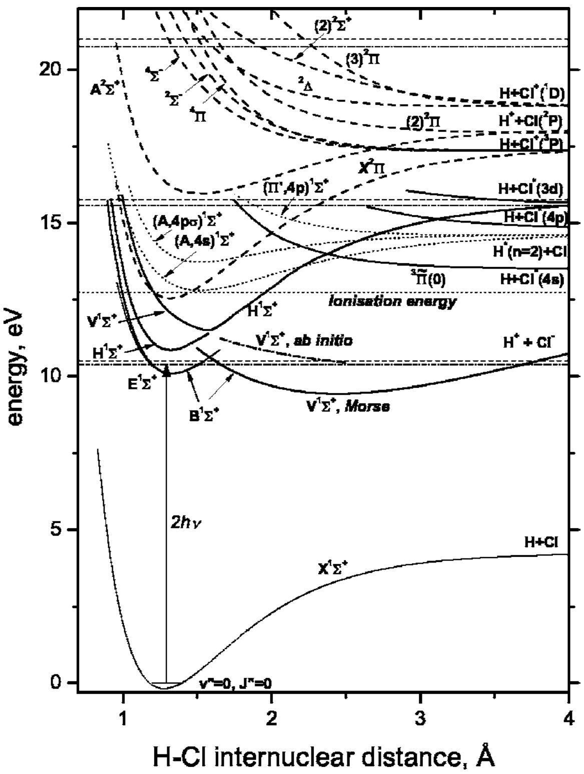

FIG. 9. Selected potential energy curves for HCl and HCl^+. Ionic states are shown by dashed curves. The states leading to $Cl+H^*(n=2)$ are shown by dotted curves. Part of the *ab initio* V state is shown by the dash-dotted curve. The horizontal lines show the ionization energy (dotted line) and the photon energies, dashed and dash-dotted for $(V,12-X,0)$ and $(E,0-X,0)$ transitions, respectively. The first two-photon step is shown by the vertical arrow.

$+Cl^*$ and H^*+Cl, which cross the three-photon energy in the vicinity of the inner turning point of the outer valence well of the B state (see Fig. 9).

We believe therefore that absorption of a third photon by HCl in the B state leads to one of two possible routes. The first is the regular route originating from the inner Rydberg well of the potential. It leads to direct ionization with $\Delta v = 0$ propensity, which is the $(2+1_i)$ pathway. The corresponding $(2+1_i+1)$ pathway, the production of H^+ from subsequent dissociation of the HCl^+ molecular ion, is negligibly small because of the small vibrational excitation of the ion. This pathway is termed regular because it is the same for all Rydberg states of a given electronic configuration, hence also occurs via the triplet states shown in Fig. 2.

TABLE IV. Morse potential parameters for $^1\Sigma^+$ states of HCl.

State	r_0 (Å)	ω_e (cm^{-1})	D^a (eV)	α^a (1/Å)
X	1.2745	2991	4.432	1.900
E	1.328^b	2547^b	4.745	1.563
V	2.441^c	773^c	4.94^c	0.465
$\sigma,\pi^4[A\ ^2\Sigma^+]4s$	1.516^d	$1538^{e,f}$	1.73^e	1.563
$\sigma,\pi^4[A\ ^2\Sigma^+]4p$	1.516^d	1384^e	0.81^e	2.056

[a] Morse potential is $U(r)=D[\exp(-2\alpha(r-r_0))-2\exp(-\alpha(r-r_0))]$, where $\alpha=(\omega_e/D)\sqrt{mD/2}$ and $m=m_H m_{Cl}/(m_H+m_{Cl})$.

[b] Reference 25.

[c] Extrapolation of the data for $v'_V=3-7$ vibrational states from Ref. 18.

[d] The value for the $HCl^+(A\ ^2\Sigma^+)$ ion from Ref. 44 is used.

[e] Reference 50.

[f] In agreement with *ab initio* calculations for $HCl^+(A\ ^2\Sigma^+)$ ion.

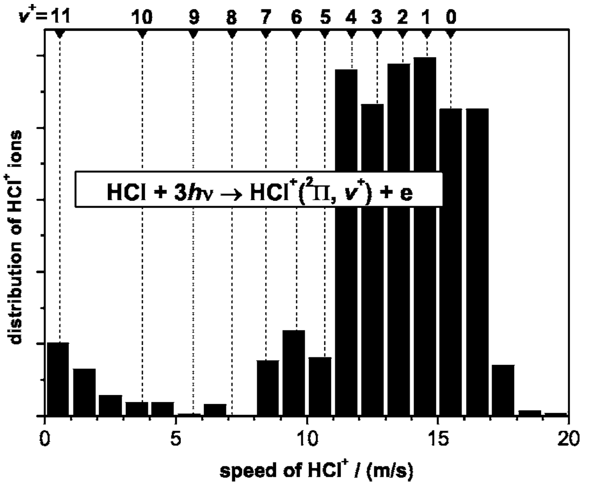

FIG. 10. $(V,12-X,0)$ transition: Distribution of HCl^+ ions over the speed. The distribution is obtained from the TOFs on Fig. 3. The vibrational states of HCl^+ ions are shown at the top of the figure. The spin-orbit structure of HCl^+ is averaged. The maximum possible speed of HCl^+ is 15.7 m/s, see Eq. (7). Due to charge effects, the broadening of the TOF profiles gives the contribution above the maximum possible speed.

The second route originates from the outer valence well of the B state and therefore is a unique feature of 0^+ states. It excites superexcited states which decay into electronically excited, neutral, and atomic species which can undergo subsequent ionization via a $(2+1+1_i)$ REMPI scheme. In other words, if Cl^+ ions are produced via REMPI $(2+1+1_i)$, they are produced through the valence well of the B state via repulsive states of HCl^{**}. This important conclusion will be used throughout this paper.

E. One-photon ionization of HCl^*

In Fig. 10 an example of the speed distribution of HCl^+ ions is presented. This energy distribution may be decomposed into the sum of contributions arising from different vibrational levels of HCl^+ $(X\ ^2\Pi, v^+)$, the corresponding energies of which are shown at the top of the figure. Note that these energies are averaged for spin-orbital states of HCl^+, except for the $v^+=11$ vibrational level, for which only the $^2\Pi_{3/2}$ state is energetically accessible. The small structure near $v^+\approx 11$ is probably due to experimental uncertainty because it was irreproducible.

The broadening of the TOF profiles yields a contribution above the maximum possible speed v_{max} calculated by Eq. (7) due to space-charge effect. From Fig. 10 it can be seen that the vibrational levels in HCl^+ are mainly populated up to $v^+\approx 4$ and that the population of higher vibrational states is negligible.

The electronic configurations of the Rydberg E and valence V contributions to the double-minimum B state of HCl are given by $(5\sigma)^2(2\pi)^3 4p\pi$ and $(5\sigma)^1(2\pi)^4(6\sigma)^1$, respectively.[57] The ground state $X\ ^2\Pi$ of HCl^+ has the configuration $^2\Pi(5\sigma)^2(2\pi)^3$, hence the direct ionization from the B state to the ground ionic state can start from the Rydberg well only.[12] The angular distributions of HCl^+ are found to be almost isotropic with average anisotropy parameters of $\beta=0.3$ and $\beta=0.2$ for $(E,0-X,0)$ and $(V,12-X,0)$ transi-

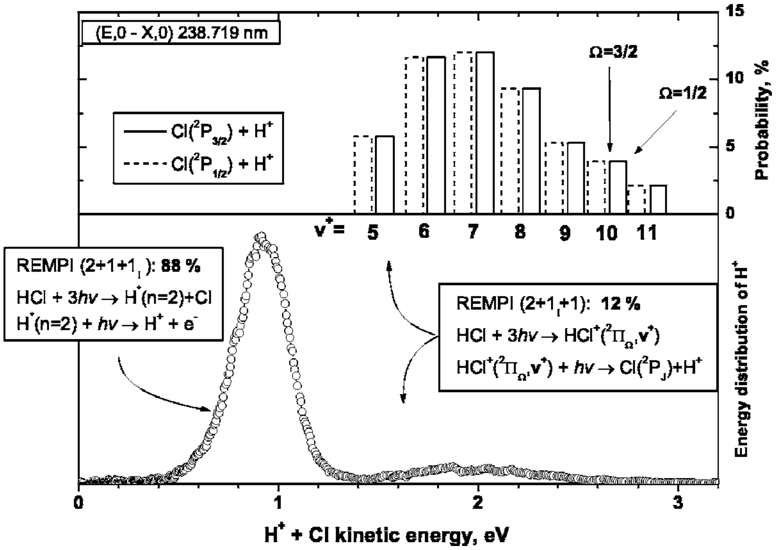

FIG. 11. Distribution of H^+ ions over the total kinetic energy of H^++Cl for the $(E,0-X,0)$ transition in $(2+1_i+1)$ and $(2+1+1_i)$ REMPI of HCl. The decomposition of the high-energy component of the distribution over the vibrational quantum number v^+ of the intermediate state $HCl^+(X\,^2\Pi_\Omega, v^+)$ is shown at the top; the probabilities are given in percent. The energy range for each v^+ corresponds to spin-orbital splittings in HCl^+ and $Cl(^2P_J)$.

tions, respectively. The parameter values are almost equal since both transitions start from the same Rydberg well.

Angle-resolved photoelectron spectroscopy of HCl was investigated in several studies. Experimental studies with photon energies from 16 to 80 eV and theoretical predictions of the β parameter were performed by Carlson *et al.*[2] The experimentally determined β parameter for the photon energy of 16 eV was found to be 0.63±0.05, in moderate agreement with our result obtained by three-photon spectroscopy.

β parameters for photoionization of simple molecules are summarized in a series of review articles on photoelectron spectroscopy.[58–61] For example, the β parameters for the photoionization of H_2, N_2, and O_2 at $h\nu=16.9$ eV are 2.0, 1.2, and −0.55, respectively.[58] In our previous study of the angular distribution of NO^+ ions due to electron recoil in the photoionization of $NO(A\,^2\Sigma_{1/2})$ at 226 nm the β parameter was close to 2,[28] in agreement with a previous PES study of Reid *et al.*[62]

In the study of Romanescu *et al.* a very detailed modeling of the vibrational distribution of HCl^+ is presented, obtained by PES for the $(E,0-X,0)$ transition.[26] A competition between direct photoionization and autoionization of HCl^+ was assumed, and the autoionization was found to be very important for $v^+=4-10$. It was also found that this autoionization occurs via the "gateway state" $^3\tilde{\Pi}_0$ which correlates to $H+Cl^*(4\,s)$. Note that it is difficult to compare our vibrational distributions with those from the PES studies in Refs. 12, 26, and 27. First, these two kinds of distributions are different, since in our case the photodissociation of HCl^+ changes the observed vibrational distribution rather strongly. Second, the energy resolution obtained from electron recoil measurements is not as high as the PES resolution.

F. Production of H^+ ions

1. Two mechanisms of production

The energy distributions of H^+ ions are presented at the bottom parts of Figs. 11 and 12 for $(E,0-X,0)$ and $(V,12-X,0)$ transitions, respectively. From the figures it can be seen that in both cases there are two groups of ions, "fast" and "slow" ones, which we denote f_f and f_s, respectively.

According to the REMPI-PES study of Romanescu *et al.*,[26] for the $(E,0-X,0)$ transition the main pathway (f_s) for the production of H^+ ions is process (5) via $H^*(n=2)$, whereas the lesser pathway (f_f) is due to processes (2) and (3), i.e., the ionization of HCl^* followed by the photodissociation of HCl^+. The same authors have reported observation of a small contribution of the ion pair channel generating $H^+ + Cl^-$ for the $(V,12-X,0)$ transition with a large β parameter of nearly 2.[63] For the main pathway the total kinetic energy of H^++Cl products may be calculated as $E'_t=3h\nu - E(H^*) - D(HCl)$, where $D(HCl)=4.4321$ eV (Ref. 64) and $E(H^*(n=2))=10.20$ eV.[65] Using this relation, we calculated the values for E'_t to be 0.92 and 1.08 eV for the $(E,0-X,0)$ and the $(V,12-X,0)$ transitions, respectively. These values agree very well with the maximum of the slow components in Figs. 11 and 12 (see Table II).

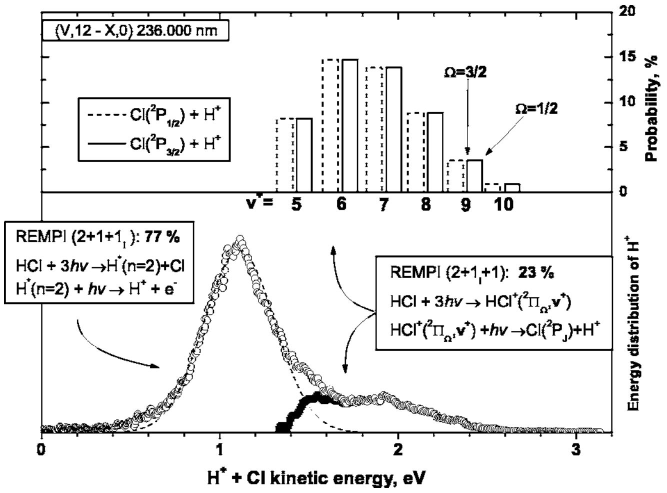

FIG. 12. Distribution of H^+ ions over the total kinetic energy of H^++Cl for the $(V,12-X,0)$ transition in $(2+1_i+1)$ and $(2+1+1_i)$ REMPI of HCl. The decomposition of the high-energy component of the distribution over the vibrational quantum number v^+ of the intermediate state $HCl^+(X\,^2\Pi_\Omega, v^+)$ is shown at the top; the probabilities are given in percent. The energy range for each v^+ corresponds to spin-orbital splittings in HCl^+ and $Cl(^2P_J)$.

For the $(V,12-X,0)$ transition, H^+ ions belonging to the ion pair channel appear at slightly higher kinetic energies than H^+ ions resulting from the ionization of H^* and are probably responsible for the incomplete separation of fast and slow H^+. In order to decompose the original distribution of H^+ ions into two components, f_f and f_s, we neglect the small ion pair contribution and assume that the distribution of H^+ ions produced in process (5) for $(V,12-X,0)$ is Gaussian, see Fig. 12. Note that the large β parameter of the ion pair channel serves to reduce the β parameter of the slow component observed in our experiment. Our $(V\text{-}X)$ β value should therefore be regarded as an upper limit to the true value.

The vibrational distribution of HCl^+ $(X\,{}^2\Pi_\Omega, v^+)$ ions was determined from f_f, as shown at the top of Figs. 11 and 12.

From the potential energy curves for HCl^+ shown in Fig. 9 it can be seen that H^+ ions may be produced through photodissociation of HCl^+ via two pathways only,

$$HCl^+(X\,{}^2\Pi_\Omega, v^+) + h\nu \rightarrow HCl^+(A\,{}^2\Sigma^+) \rightarrow H^+ + Cl(^2P_J) \tag{3a}$$

$$\rightarrow HCl^+((2)^2\Pi) \rightarrow H^+ + Cl(^2P_J). \tag{3b}$$

The first step here is a one-photon dipole allowed transition to one of the two excited states of HCl^+; the second step is a decay of the excited state.

There are several arguments in favor of pathway (3b) via the repulsive $(2)^2\Pi$ state. This pathway is only possible for vibrational levels with $v^+ \geqslant 5$ (see Fig. 13) as observed in the experiment. On the other hand, the pathway via the bound $A\,{}^2\Sigma^+$ would be available for all vibrational states of HCl^+ (X, v^+), except the specific case of $v^+=0$ and $\Omega=3/2$. This pathway can be excluded because dissociation of HCl^+ $(X, v^+=0,1)$ via excitation of pure Rydberg states is negligible. The decomposition of the H^+ energy distributions f_f over the vibrational number v^+ in the photodissociation (3) is shown at the top of Figs. 11 and 12. According to this decomposition, H^+ ions are produced from $v^+ \geqslant 5$ vibrational states of HCl^+ (X, v^+). These vibrational distributions of HCl^+ $(X\,{}^2\Pi_\Omega, v^+)$ also favor the pathway via the $(2)^2\Pi$ state. Note that the lower spin-orbit state ${}^2\Pi_{3/2}$ of the $v^+=5$ vibrational state does not have enough energy to participate in the photodissociation (see Fig. 13), which explains why the contribution from $v^+=5$ is two times smaller than the contributions from the $v^+=6$, 7 states.

In support of the assignment of the f_f peaks to pathway (3b) we can also argue that, first, the energy difference between $X\,{}^2\Pi$ and $A\,{}^2\Sigma$ states is never equal to the photon energy (see Fig. 13), which must strongly decrease the probability of the transition between these states. Second, the transition moment for the $X\,{}^2\Pi \rightarrow (2)^2\Pi$ transition is rather large ($\sim$0.4 a.u.), much larger than the transition moment for the $X\,{}^2\Pi \rightarrow A\,{}^2\Sigma$ transition for all possible internuclear distances.[44,52]

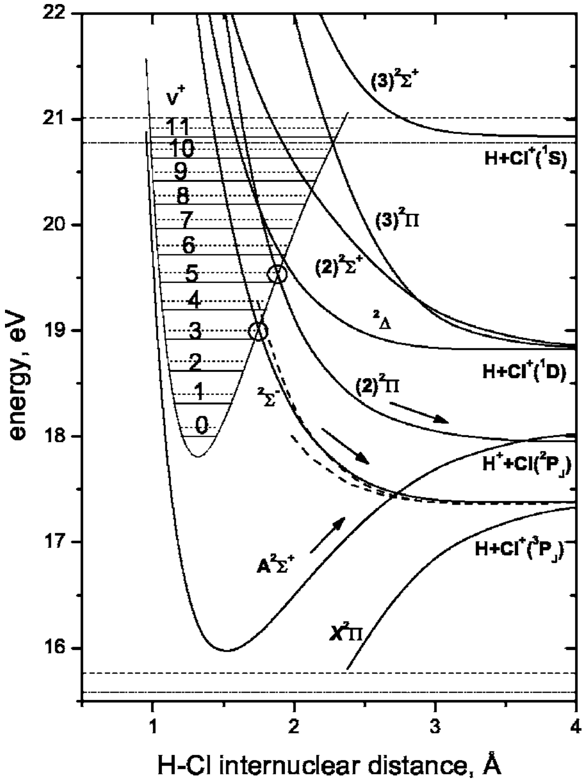

FIG. 13. Potential energy curves for HCl^+ (part of Fig. 9). The horizontal dashed and dashed-dotted lines show the photon energies for $(V,12-X,0)$ and $(E,0-X,0)$, respectively. The vibrational levels of $HCl^+(X, {}^2\Pi, v^+)$ are upshifted by an amount of the laser photon energy for $(V,12-X,0)$ transition; they are shown by solid and dashed lines for ${}^2\Pi_{3/2}$ and ${}^2\Pi_{1/2}$ spin-orbit states, respectively. For $(E,0-X,0)$ the levels must be downshifted by 0.06 eV. ${}^4\Pi$ and ${}^4\Sigma$ states are shown by dashed curves. The arrows show pathways for H^+ and Cl^+ production; the circles mark the areas on the repulsive surfaces from where these ions are likely to be produced via $(2+1_i+1)$ REMPI. The picture illustrates that the photodissociation channels $HCl^+(v^+)+h\nu \rightarrow Cl+H^+$ and $HCl^+(v^+)+h\nu \rightarrow Cl^+ + H$ are possible only for $v^+ \geqslant 5$ and $v^+ \geqslant 4$ vibrational states, respectively.

2. Vibrational distribution consideration

Considering the above mechanisms the vibrational distribution of HCl^+ ions after the ionization step (2) can be explained. According to Fig. 13, only those HCl^+ ions will be photolyzed which have large vibrational excitation with $v^+ \geqslant 5$ and $v^+ \geqslant 4$ for channels (3) and (4), respectively. If HCl^+ ions have a lower vibrational excitation, they will not be photolyzed, and their vibrational distribution may be obtained from the speed distribution of HCl^+ ions, see Fig. 10. It is difficult to restore the "initial" distribution of HCl^+ after the ionization step (2), because it is a combination of distributions obtained from the analysis of HCl^+, Cl^+, and H^+ speed distributions.

Note that such initial vibrational distributions of HCl^+ ions were obtained from the PES of HCl by Romanescu *et al.* for several electronic-vibrational transitions, including the transition $(E,0\text{-}X,0)$.[26] These distributions are relatively smooth and extend to $v^+=11$, without any irregularity near $v^+=4-5$.

This mechanism also explains why no H^+ is produced following the direct photoionization of HCl into HCl^+ $(X, v^+=0,1)$ via pure Rydberg states.

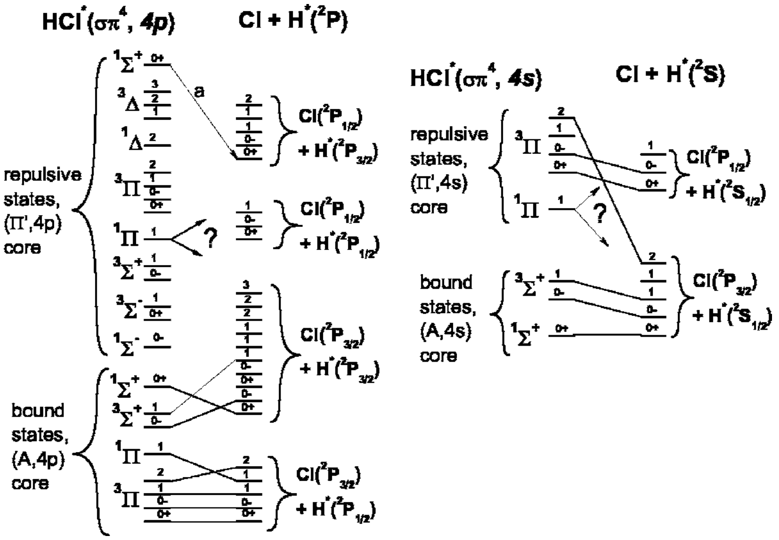

FIG. 14. Correlation diagrams for production of “slow” H^+ ions. Left: The repulsive $^1\Sigma^+$ state (labeled “a”) is assumed to be σ^* orbital and hence it is the highest among states with 0^+ projection. The order of other repulsive states is usually unknown, hence it is unclear, if repulsive $^1\Pi_1$ terms produce $Cl^*(^2P_{1/2})$ or $Cl(^2P_{3/2})$. These uncertainties are labeled by “?.”

3. Anisotropy parameter consideration

a. Slow H^+ *ions*. In the study of Romanescu *et al.* the β parameters determined by REMPI of H^+ ions are 0.9 and −0.2 for channels (5a) and (5b) respectively:[26]

$$HCl^*(B\,^1\Sigma^+) \xrightarrow{+h\nu} HCl^{**}$$

$$\rightarrow Cl(^2P_{1/2}) + H^* \xrightarrow{+h\nu} Cl + H^+ + e^- \tag{5a}$$

$$\rightarrow Cl(^2P_{3/2}) + H^* \xrightarrow{+h\nu} Cl + H^+ + e^-. \tag{5b}$$

In their follow-up study Manzhos *et al.* have revised the value to be 1.04, taking higher order contributions into account,[27] whereas we have obtained $\beta = 1.23$. This seeming contradiction might be resolved as follows. We have used the rotational transition $Q(0)$ which produces HCl^* isotropically, unaffected from alignment effects. Loock and co-workers have used the $Q(1)$ transition, which produces aligned HCl^* in the two-photon transition (1). The study of this alignment effect based on the comparison of angular distributions of H^+ ions for the transitions $Q(0)$ and $Q(1)$ is under way and will be published in a forthcoming article.

According to de Beer *et al.* and Loock and co-workers, the slow H^+ ions are produced via a one-photon transition to the superexcited $HCl^{**}(^1\Sigma^+)$ state above its dissociation limit in process (5). The optical transition $^1\Sigma^+ \rightarrow {}^1\Sigma^+$ in the excited HCl molecule is parallel ($\Delta\Omega = 0$) with a maximal anisotropy parameter of $\beta = 2$. Our observed experimental values for the β parameters for these f_s peaks are 1.23 and 0.90 for $(E,0\text{-}X,0)$ and $(V,12\text{-}X,0)$ transitions, respectively. This difference cannot be explained by quick rotation of the HCl^* molecule, since it is in the rotational state $J' = 0$. Thus we can conclude that the upper superexcited state is not of pure $^1\Sigma^+$ symmetry, but that there must be an impurity of another state with $\Omega = 1$, which is probably the nearest superexcited state $^1\Pi(1)$. The relative contribution of the perpendicular component is calculated to be $X_\perp = 0.26$ and $X_\perp = 0.37$ for $(E,0\text{-}X,0)$ and $(V,12\text{-}X,0)$ transitions, respectively. The standard relationships $\beta = \beta_\perp X_\perp + \beta_\parallel X_\parallel$, $X_\perp + X_\parallel = 1$, $\beta_\perp = -1$, and $\beta_\parallel = 2$ are used in this calculation. Thus, the contributions of the perpendicular component are different for different electronic-vibrational transitions. This is probably due to the difference in energy of the photons or/and the width of the Franck-Condon region, which in the case of the $(V,12\text{-}X,0)$ transition is much broader than the $(E,0\text{-}X,0)$ transition.

Manzhos *et al.*[27] have fitted their experimental angular distributions of slow H^+ ions obtained for the $(E,0\text{-}X,0)$, $Q(1)$ transition by several models, labeled from A to G. The best fit to experimental data was obtained with model A, which assumes a purely perpendicular two-photon step (1) followed by a purely parallel step (5). However, the model F which assumes a small ($X_\perp = 0.08$) perpendicular contribution to the dissociative step of (5) was found to yield an almost equally good agreement with the experimental data. We have evidence that the last step (5) is not purely parallel, and hence suggest that the model F of Manzhos *et al.* should be used, with our value $X_\perp = 0.26$.

Generally, alignment[66] and orientation[67] of the molecule in the molecular beam can contribute to optical alignment. Three-dimensional imaging is a more powerful tool to recognize and account for such effects than two-dimensional (2D) imaging techniques, since alignment and orientation in the molecular beam may be checked and studied by comparison of angular distributions obtained in two configurations, $\boldsymbol{E} \parallel \boldsymbol{Y}$ and $\boldsymbol{E} \perp \boldsymbol{Y}$, where Y is directed along the molecular beam.

b. Fast H^+ *ions*. The production of fast H^+ ions in the peak f_f is due to process (3b), in which the photodissociation step is the one-photon transition $^2\Pi \rightarrow {}^2\Pi$ in the HCl^+ ion. This transition must be mainly parallel also. The β parameters for fast H^+ ions are 1.6 for both $(E,0\text{-}X,0)$ and $(V,12\text{-}X,0)$ transitions. The decrease of the β parameters from the limiting value of 2 can be explained either by the contribution of the perpendicular transition (3a), or by $^2\Pi_{3/2} \leftrightarrow {}^2\Pi_{1/2}$ transitions.

4. Pathway consideration

It is usually assumed that slow H^+ ions are produced mainly via $^1\Sigma^+$ terms correlating with $H^*(n=2) + Cl$.[12,27] According to Table III and Fig. 14, there are three such $^1\Sigma^+$

terms,

$$\mathrm{HCl}^*(B) + h\nu \to \mathrm{HCl}^{**}(\Pi', 4p\pi\ {}^1\Sigma^+) \to \mathrm{Cl}({}^2P_{1/2}) + \mathrm{H}^*({}^2P), \tag{8a}$$

$$\mathrm{HCl}^*(B) + h\nu \to \mathrm{HCl}^{**}(A, 4s\ {}^1\Sigma^+) \to \mathrm{Cl}({}^2P_{3/2}) + \mathrm{H}^*({}^2S), \tag{8b}$$

$$\mathrm{HCl}^*(B) + h\nu \to \mathrm{HCl}^{**}(A, 4p\sigma\ {}^1\Sigma^+) \to \mathrm{Cl}({}^2P_{3/2}) + \mathrm{H}^*({}^2P). \tag{8c}$$

Romanescu *et al.*[26] have found that the yield of ground state chlorine $\mathrm{Cl}({}^2P_{3/2})$ is very small, i.e., the atoms are mainly produced in the spin-orbit excited state $\mathrm{Cl}^*({}^2P_{1/2})$. One can see from the correlation diagrams that channels (8b) and (8c) lead to ground state atoms, while only channel (8a) leads to $\mathrm{Cl}({}^2P_{1/2})$, see Fig. 14. Thus, we give strong preference to channel (8a). Besides, this conclusion leads to the prediction that $[\mathrm{H}^*({}^2P)] \gg [\mathrm{H}^*({}^2S)]$. The small perpendicular component is probably due to the excitation of the repulsive ${}^1\Pi_1$ term.

The ground state atoms $\mathrm{Cl}({}^2P_{3/2})$ are produced with $\beta = -0.2$.[26] Since β is negative, these chlorine atoms are produced probably due to ${}^1\Pi_1$ terms. According to Table III and Fig. 14, there are three such terms, one is bound and two are repulsive,

$$\mathrm{HCl}^*(B) + h\nu \to \mathrm{HCl}^{**}(A, 4p\pi\ {}^1\Pi_1) \to \mathrm{Cl}({}^2P_{3/2}) + \mathrm{H}^*({}^2P), \tag{9a}$$

$$\mathrm{HCl}^*(B) + h\nu \to \mathrm{HCl}^{**}(\Pi', 4s\ {}^1\Pi_1) \to \mathrm{Cl}^*/\mathrm{Cl} + \mathrm{H}^*({}^2S), \tag{9b}$$

$$\mathrm{HCl}^*(B) + h\nu \to \mathrm{HCl}^{**}(\Pi', 4p\sigma\ {}^1\Pi_1) \to \mathrm{Cl}^*/\mathrm{Cl} + \mathrm{H}^*({}^2P). \tag{9c}$$

Note that channels (9c) and (9b) may not produce $\mathrm{Cl}({}^2P_{3/2})$ atoms, since we do not know, where the repulsive ${}^1\Pi_1$ terms correlate to, see Fig. 14.

G. Cl$^+$ ions

In the PES spectra published by de Beer *et al.*[12] and by Romanescu *et al.*,[26] there are several groups of peaks which are assigned to the photoionization of $\mathrm{Cl}^*({}^3P4s)$, $\mathrm{Cl}^*({}^3P4p)$), and $\mathrm{Cl}^*({}^3P3d)$ excited atoms, but no attempts have been made to identify the superexcited HCl^{**} states responsible for this fragmentation. Based on our observed kinetic energy distributions and anisotropy parameters we are able to point out the most likely target states. The kinetic energies of $\mathrm{H}+\mathrm{Cl}^+$ products for REMPI $(2+1+1_i)$ pathways (6) for different electronic states of Cl^* atoms are shown at the top of Fig. 15, in which we present our kinetic energy distributions of Cl^+ ions. As follows from the figure, there is a good agreement with the PES data.

Before pathway consideration we should note that the quantitative discussion of the angular distributions of Cl^+ may be complicated because the Cl^* atoms obtained in the processes (6) may be aligned due to v-j correlation. If this alignment takes place, the probability of the photoionization of these atoms becomes angular dependent, and a simple interpretation of the β parameters becomes impossible. Since the ionization step can be expected to be saturated, this alignment is unlikely to play a significant role and has consequently been neglected in our analysis.

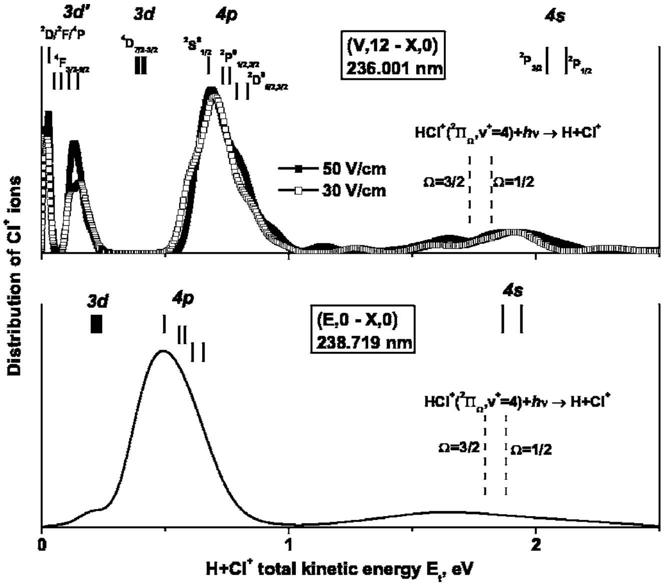

FIG. 15. Distribution of Cl^+ ions over the total kinetic energy of the $\mathrm{H}+\mathrm{Cl}^+$ system. For the $(V,12-X,0)$ transition two distributions obtained for different acceleration voltages are shown. The energies for REMPI $(2+1+1_i)$ pathways (6) for selected electronic states of Cl^* atoms are shown at the top. At the right side we also show the kinetic energies for REMPI $(2+1_i+1)$ pathway (11).

All possible superexcited target states can be constructed from ionic curves correlating to $\mathrm{H}+\mathrm{Cl}^+$ by adding the corresponding nl electron. Due to energetic reasons only ionic curves correlating to the $\mathrm{Cl}^+({}^3P)$ and $\mathrm{Cl}^+({}^1D)$ need to be considered. The system $\mathrm{H}+\ \mathrm{Cl}^+({}^3P)$ can completely be described by a set of four potential energy curves, namely, by one bound state ($\mathrm{HCl}^+[X\ {}^2\Pi]$) and by three repulsive states (${}^2\Sigma^-$, ${}^4\Sigma^-$, and ${}^4\Pi$). The system $\mathrm{H}+\mathrm{Cl}^+({}^1D)$ is exclusively correlated to three repulsive states (${}^2\Sigma^+$, ${}^2\Pi$, and ${}^2\Delta$).

Adding an nl electron to the ionic potentials described above one obtains quite a large number of neutral, superexcited Rydberg states which can, in principle, act as target states for excitation from the outer well of the B state. Fortunately, as will be shown in the following, most of these states can be excluded for a number of reasons. The corresponding discussion will in detail be presented for the case of the 4*s* Rydberg system and can be applied in the same manner to all other *nl* systems as well. Of course, the number of states which need to be considered in this procedure significantly increases with the orbital angular momentum of the Rydberg electron.

1. HCl*(B)+$h\nu$→HCl**→H+Cl*: *Criteria for pathway assignment*

Without detailed quantum chemical calculations, in order to evaluate the role of the individual states in Cl^+ production we have four criteria at hand.

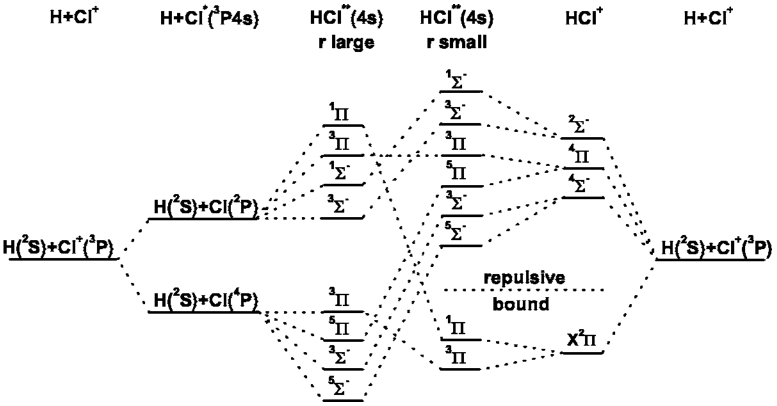

FIG. 16. Correlations between the Rydberg states of the HCl** molecule and the electronic states of the separated excited atoms, illustrated for Cl*(4*s*). Outer columns start with the separated ionic states. From the left, first the 4*s* electron is added to the Cl$^+$ ion, from which the Rydberg molecule is constructed. The energetic ordering for the Cl*(4*s*) doublet and quartet systems is preserved for the Rydberg molecule at large internuclear distances, while the ordering within the systems is unknown. From the right, first the molecular ion is combined resulting in one bound and three repulsive states. Adding the 4*s* electron now results in molecular Rydberg states at small internuclear distances.

First, we will focus our attention on repulsive Rydberg states of HCl** only. This criterium is based on the experimental observation that pure Rydberg states exclusively lead to ionization. If the bound Rydberg states played a role in the $\mathrm{HCl}^*(B)+h\nu\rightarrow\mathrm{HCl}^{**}\rightarrow\mathrm{H}+\mathrm{Cl}^*$ process, then it cannot be conceived why excitation of pure Rydberg states in the first two-photon absorption step should not produce neutral fragments as well, but only molecular ions. Also, the bound Rydberg states $\mathrm{HCl}^{**}([X\,^2\Pi]nl)$ are unlikely to be accessed in the absorption of the third photon because the shape of their potential is similar to the ionic states which are directly accessed in the regular $(2+1_i)$ ionization process.

Second, from experiment we know the spatial distribution of the fragments under consideration, so we can draw conclusions on the projection of the total angular momentum as given by the quantum number Ω. For pure parallel transitions the β parameter is +2, and the target state must have $\Omega=0$, while for perpendicular transitions the β parameter is -1, and the target state must have $\Omega=1$. In particular, we will always neglect transitions with $|\Delta\Omega|>1$.

Third, we can evaluate whether transitions are electric dipole allowed or not. This criterium strongly prefers singlet target states $(\Delta S=0)$ over triplet target states $(\Delta S=1)$ and triplet target states over quintet target states $(\Delta S=2)$. No other multiplicities play a role within the current discussion. Some forbidden transitions occur due to spin-orbit interaction, which mixes singlet and triplet states. For example, the $B\,^1\Sigma^+$ state has impurities of the $b\,^3\Pi_0$ and the $g\,^3\Sigma_0^-$ states.[68] Consequently, singlet-triplet transitions as well as $\Sigma^+\rightarrow\Sigma^-$ transitions need to be taken into account.

Last, the number of electrons that need to be transferred from one orbital to another for a given transition can be counted. Two-electron promotion can, in general, be regarded as much less likely than a one-electron promotion. We are aware that this last criterium makes use of a single configuration description which is not appropriate for the strongly perturbed *B* state in general. However, at large internuclear distances the *B* state is essentially the pure *V* ion pair state, and the argument becomes applicable.

2. Fast Cl$^+$ ions via REMPI $(2+1+1_i)$

We know from high-resolution PES (Refs. 12 and 50) and REMPI (Ref. 26) studies that the fast Cl* ions at $E_t\approx 2$ eV are produced via pathway (6) through ionization of Cl*(4*s*). In all previous studies[12,26,50] the production of Cl*(4*s*) fragments was assigned to the HCl**($^3\tilde{\Pi}_0$) intermediate state,

$$\mathrm{HCl}^*(B)+h\nu\rightarrow\mathrm{HCl}^{**}(^3\tilde{\Pi}_0)\rightarrow\mathrm{H}+\mathrm{Cl}^*(4s). \tag{10}$$

This assignment agrees with our conclusion. Let us demonstrate the logics based on the above mentioned criteria as illustrated in Fig. 16. According to Table III, the H $+\mathrm{Cl}^*(4s)$ system correlates to two bound molecular states $^{1,3}\Pi$ and to six repulsive molecular states $^1\Sigma^-$, $^3\Sigma^-(2)$, $^3\Pi$, $^5\Sigma^-$, and $^5\Pi$ as is shown in Fig. 16. For the fast Cl atoms β parameters of 1.6±0.3 for *V* state excitation and of 1.9±0.2 for *E* state excitation were determined. Thus, the corresponding transitions must essentially be parallel, corresponding to the condition $\Delta\Omega=0$. For the reason given above, bound states need not be considered. Of the repulsive states, only $^1\Sigma^-(0^-)$, $^3\Sigma^-(0^+)$, and $^3\Pi_0$ exhibit the required $\Omega=0$ quantum number if we neglect quintet states. With $\sigma\pi^4\sigma^*$ being the electronic configuration of the $V\,^1\Sigma^+$ state, only the transition to Π can be realized by a one-electron $\pi\rightarrow 4s$ excitation, whereas excitation of any Σ^- state requires a two-electron $(\pi\rightarrow 4s, \pi\rightarrow\sigma)$ promotion. Since all transitions originating from $^1\Sigma^+$ to these states are forbidden for one-photon electric dipole radiation, no preference can be given to any one of them based on the selection rule criterion. In conclusion, the most likely excitation responsible for the production of Cl*(4*s*) fragments proceeds via the $^3\tilde{\Pi}_0$ state. The comparatively low intensity of the corresponding peak in the kinetic energy distribution may owe to the singlet-triplet character of the excitation.

Nevertheless, it must be considered that in their majority at short nuclear distances the doublet surfaces of the molecular ion have lower energies than their quartet counterparts, whereas the opposite is true for the atomic states of the excited chlorine atom, i.e., for large nuclear distances. Hence, for any manifold there exists a certain number of avoided crossings which occur at intermediate nuclear distances, which is where the absorption of the third photon takes place from the outer well of the $B\,^1\Sigma^+$ state.

Note also that correlation rules predict that chlorine atoms produced via the $^3\tilde{\Pi}_0$ term must be in the lower state of the fine structure $^2P_{3/2}$ only, in agreement with experiment.[12]

3. Fast Cl$^+$ *ions via REMPI* $(2+1_i+1)$

The fast Cl$^+$ ions may also be produced by photodissociation of HCl$^+$ ions via REMPI $(2+1_i+1)$ pathway (4). According to Fig. 13, there exists the pathway

$$\mathrm{HCl}^+(^2\Pi_\Omega, v^+ \geqslant 4) + h\nu \rightarrow \mathrm{HCl}^{**}(^2\Sigma^-) \rightarrow \mathrm{H} + \mathrm{Cl}^+, \quad (11)$$

which must produce Cl$^+$ ions with sufficient probability. This pathway has never been discussed before. At Fig. 15 we show the kinetic energies of H+Cl$^+$ products for this pathway. According to the figure, pathways (10) and (11), which correspond to $(2+1+1_i)$ and $(2+1_i+1)$ REMPI schemes, produce fast Cl$^+$ with nearly the same energy.

Note that while pathway (11) must result in a rather broad distribution of H+Cl$^+$ products over kinetic energy because of the distribution of HCl$^+$ over v^+, pathway (10) gives a narrow energy distribution. Unfortunately, the resolution of our spectrometer is not sufficient to distinguish between them, see Fig. 7.

It is difficult to estimate the relative contribution of these two pathways, but nevertheless we give preference to pathway (10). First, in the PES spectra of de Beer *et al.* a rather strong signal from Cl$^+$ ions produced via pathway (10) is presented.[12] That is, the contribution from pathway (10) is surely large. Second, the β parameters for the "fast" Cl atoms are large and positive. This is normal for pathway (10), but it assumes a strong preference of $^2\Pi_{1/2}$ spin-orbital states of HCl$^+$ over $^2\Pi_{3/2}$ states for pathway (11). We do not see any reason for such a preference.

4. Slow Cl$^+$ *ions*

The slow Cl$^+$ ions at 0.7 eV for the $(V,12-X,0)$ transition and at 0.56 eV for the $(E,0-X,0)$ transition are produced via pathway (6).[12,26]

In more detail, these slow Cl$^+$ ions can be produced by two different Rydberg configurations of HCl**. One is obtained by adding a $4p$ electron to the Cl$^+$(^3P) core, the other one by adding a $4s$ electron to the Cl$^+$(^1D) core. These excited states are denoted Cl*($4p$) and Cl*($4s'$), respectively. Both configurations give rise to a system of molecular states which cannot be distinguished on the basis of kinetic energy measurements within experimental resolution of our setup. De Beer *et al.* have assigned PES peaks to ^2D and ^2S states of Cl*($4p$) atoms,[12] but the presence of ^2P states is also evident because of the strong mixing between the ^2D, ^2S, and ^2P states. The PES study of de Beer *et al.* shows that the production of Cl*($4s'$) is a minor channel from evaluating the unassigned peak at ca. 1.2 eV in their Fig. 4.

As follows from Table III, the system H+Cl*($4p$) correlates to eight bound states and to 16 repulsive states ($^{1,3}\Sigma^-([^2\Sigma^-]4p\sigma)$, $^{1,3}\Pi([^2\Sigma^-]4p\pi)$, $^{3,5}\Sigma^-([^4\Sigma^-]4p\sigma)$, $^{3,5}\Pi([^4\Sigma^-]4p\pi)$, $^{3,5}\Sigma^+([^4\Pi]4p\pi)$, $^{3,5}\Sigma^-([^4\Pi]4p\pi)$, $^{3,5}\Pi([^4\Pi]4p\sigma)$, and $^{3,5}\Delta([^4\Pi]4p\pi)$). Again, bound states will not be considered. Contrary to the previously discussed case of fast Cl ions, now there exists a one-photon electric dipole allowed transition, namely, into $^1\Pi([^2\Sigma^-]4p\pi)$. On the other hand, this transition involves the promotion of two electrons. The only available one-electron excitation scheme accesses the $[^4\Pi]4p$ manifold. Ruling out all quintet and the $^3\Delta$ states, one obtains for dipole-forbidden one-electron excitation the states $^3\Sigma^-$, $^3\Sigma^+$, and $^3\Pi$ as targets; we denote them as $^3\Lambda$. Finally, the Cl*($4p$) atoms can be produced by the following four pathways:

$$\mathrm{HCl}^*(B) + h\nu \rightarrow \mathrm{HCl}^{**}\ (^1\Pi([^2\Sigma^-]4p\pi))) \rightarrow \mathrm{H} + \mathrm{Cl}^*(4p) \quad (12a)$$

$$\rightarrow \mathrm{HCl}^{**}(^3\Lambda([^4\Pi]4p)) \rightarrow \mathrm{H} + \mathrm{Cl}^*(4p). \quad (12b)$$

Following the same arguments, the system H+Cl*($4s'$) only correlates to six repulsive states $[^{1,3}\Sigma^+([(2)^2\Sigma^+]4s)$, $^{1,3}\Pi([(3)^2\Pi]4s)$, and $^{1,3}\Delta^-([^2\Delta]4s)]$. Here, the Π states correspond to a one-electron excitation, while only $^1\Sigma^+$ and $^1\Pi$ are dipole allowed. Thus, the most likely candidate here is the process

$$\mathrm{HCl}^*(B) + h\nu \rightarrow \mathrm{HCl}^{**}(^1\Pi([(3)^2\Pi]4s)) \rightarrow \mathrm{H} + \mathrm{Cl}^*(4s'). \quad (13)$$

Note that channels (12a) and (13) include perpendicular optical transitions with $\Delta\Omega=1$, hence one would expect $\beta=-1$ for the angular distribution of Cl* atoms. However, the experimentally observed β values are 0.41 ± 0.3 and 1.4 ± 0.1 for the $(V,12-X,0)$ and $(E,0-X,0)$ transitions, respectively. Hence the contribution of "parallel" transitions in channel (12b) must be large, 0.47 ± 0.1 and 0.80 ± 0.04, respectively. Nevertheless, the significantly smaller β parameter of the slow Cl ions as compared to the fast ones discussed before is evidence of additional contribution of a perpendicular transition. A larger number of target states is also consistent with the large total yield of the slow ions.

Again, avoided crossings for states of equal symmetries at intermediate nuclear distances may serve to enhance the probability for the occurrence of multiplet changing transitions.

5. "Very slow" Cl$^+$ *ions*

In the case of the $(V,12-X,0)$ transition there is a group of very slow ions. This very slow group consists of two components, at 0.13 and 0.02 eV. This structure is reproducible, which is confirmed by measurements at different acceleration voltages, see Fig. 15.

In these experiments the energy of three photons is enough to produce ^4P, $^{2,4}F$, and $^{2,4}D$ states of Cl*($3d,3d'$) atoms, but not ^2P of Cl*($3d''$). The system H+Cl*($3d,3d',3d''$) correlates to 12 bound states, of which six are singlet and six are triplet, and 24 repulsive states, of which three are singlet, 12 are triplet, and nine are quintet.

The lowest term of Cl*($3d$) is ^4D. It lies far enough below the next higher ^4F state that ions belonging to these two states can easily be distinguished from each other by their kinetic energy. From Fig. 15 it can be seen that no Cl ions in ^4D are observed, instead ^4F (and higher lying states) are populated. This behavior is evident because the ^4D state exclusively correlates to bound triplet states and to repulsive quintet states. With the exception of a repulsive $^3\Delta$, state the situation is the same for the ^4F state. However, as will be discussed below, the ^4F state significantly differs from its ^4D counterpart in that it shows a strong admixture of the ^2F state while ^4D is essentially pure.

The best candidates for target states in the $\mathrm{Cl}^*(3d')$ manifold are obviously the three repulsive singlet states $^1\Sigma^-$, $^1\Pi$, and $^1\Delta$. The last will not be accessed because $\Delta\Lambda=2$, and the former two correlate to $\mathrm{H}+\mathrm{Cl}^*(3d'')$, which lies above the three-photon energy threshold. Thus, no repulsive singlet state should play a significant role in the production of $\mathrm{H}+\mathrm{Cl}^*(3d')$. Instead, the likeliest candidates are again triplet states arising from the $^4\Pi$ core of HCl^+ because it is the only one requiring a one-electron excitation $\pi\rightarrow 3d$,

$$\mathrm{HCl}^*(B)+h\nu\rightarrow \mathrm{HCl}^{**}(^3\Lambda'([^4\Pi]3d))\rightarrow \mathrm{H}+\mathrm{Cl}^*(3d'), \tag{14}$$

here $^3\Lambda'$ denote two $^3\Pi$ states and a $^3\Sigma^+$ and a $^3\Sigma^-$ state, while $^3\Delta$ and $^3\Phi$ may be excluded. It is clear from the kinetic energy that the ions with the energy near 0.13 eV are due to these processes. Since the energetic order of the molecular repulsive states is not known, these four states can adiabatically correlate to the production of $\mathrm{H}+\mathrm{Cl}^*(3d')$ either in ^4P, ^2F, or ^2D. ^2D and ^4P are known to be strongly mixed. The same is true for ^2F and ^4F, which is why we observe a kinetic energy at the position corresponding to $\mathrm{Cl}^*([^4F]3d')$ although it cannot be directly accessed within the mechanism presented here.

Note that in the discussion of the Cl^+ pathways we always excluded bound states of HCl^{**}. This rule is based on Franck-Condon arguments and it may have one exception. The very slow $\mathrm{Cl}^*(3d')$ atoms may be produced via the optical transition from $\mathrm{HCl}^*(B)$ to one of the bound states of HCl^{**} which correlates to $\mathrm{Cl}^*(3d')$ at very large internuclear distances where repulsive and bound states of HCl^{**} almost coincide. According to Table III, among the bound states leading to $\mathrm{Cl}^*(3d')$ there are only three which are singlet-singlet and electric dipole allowed; they are $^1\Sigma^+$, $N\,^1\Pi$, and $K\,^1\Pi$. The experimentally observed transition is mainly parallel, $\beta=1.48\pm0.2$, and hence only state $H\,^1\Sigma^+$ must be taken into account. From correlation analysis it is known that the state $\mathrm{HCl}^{**}(H\,^1\Sigma^+)$ correlates to the $\mathrm{Cl}(^2D_{5/2}\,3d')$ state. Thus, the very slow ions with the energy of 0.02 eV could also be due to the process

$$\mathrm{HCl}^*(B)+h\nu\rightarrow \mathrm{HCl}^{**}(H\,^1\Sigma^+)\rightarrow \mathrm{H}+\mathrm{Cl}^*(^2D_{5/2}\,3d'). \tag{15}$$

6. Common features for Cl* *production*

Finally, the total yields of $\mathrm{Cl}^*(3d')$, $\mathrm{Cl}^*(4p)$, and $\mathrm{Cl}^*(4s)$ are of comparable magnitude. All three fragmentation channels have in common that dipole-allowed transitions have minor contribution to their realization. Instead singlet-triplet excitation to repulsive states of HCl^{**} with a $^4\Pi$ core must be mainly responsible for product species. Another common feature of these three channels is their positive β parameter, although in view of the small kinetic energy release for the $\mathrm{Cl}^*(3d')$ fragments, this observation should not be overinterpreted. We assume that these singlet-triplet transitions are enhanced by the impurity of the $b\,^3\Pi_0$ state to $B\,^1\Sigma^+$ state due to spin-orbit interaction.[68] This impurity must be very large at the internuclear distance where these two states cross each other, somewhere at the inner side of the valence well of the V state; at other internuclear distances this mixing must be relatively small.

The $^3\Pi_{\pm1}$ states do not play a role, neither as impurities to the $B\,^1\Sigma^+$ state nor as target states for transitions from $B\,^1\Sigma^+$. In the first case, spin-orbit interaction does not occur between $b\,^3\Pi_{\pm1}$ and $B\,^1\Sigma^+$ states due to the selection rule $\Delta\Omega=0$. In the second case, in Hund's case *a* the optical transitions $^3\Pi_0\rightarrow{}^3\Pi_{\pm1}$ are forbidden and the transitions $^3\Pi_0\rightarrow{}^3\Pi_0$ are allowed.

V. SUMMARY

The photodissociation and photoionization of state-prepared $\mathrm{HCl}(B\,^1\Sigma^+, J'=0)$ molecules has been studied in detail by 3D imaging, where H^+, Cl^+, and HCl^+ ions have been analyzed with respect to the speed distributions and anisotropy parameters. The pathways and the β parameters which have been observed in the present study are presented in Fig. 8. The results may be summarized as follows.

The velocity (speed and angle) distributions of HCl^+ ions due to the electron recoil have been determined. These distributions yield β parameters and vibrational distributions of HCl^+, which allow to study the photoionization process itself and also the photodissociation of HCl^+.

HCl^+ ions are produced from HCl by absorption of three photons with a broad vibrational distribution, $0\leqslant v^+\leqslant 11$,[26] mainly resulting from autoionization. Vibrationally hot ($v^+\geqslant 4-5$) ions are mainly photolyzed and produce H^+ ions and possibly Cl^+ ions. HCl^+ is not photolyzed if it is vibrationally cold ($v^+\leqslant 4-5$). This is derived from TOF distributions of H^+ and HCl^+.

The β parameters and the speed distributions of H^+ and Cl^+ ions produced by four-photon absorption in HCl have been determined. The speed distributions are in agreement with those obtained recently by REMPI-PES,[26] whereas the β parameters for $Q(0)$ rotational transitions are obtained for the first time. These β parameters are the most suitable for the analysis of photoionization and photodissociation of excited state HCl^* because they eliminate alignment effects in HCl^*.

Two pathways in production of H^+ ions, via REMPI$(2+1_i+1)$ and REMPI$(2+1+1_i)$, have been confirmed. In the first case, the pathway through $\mathrm{HCl}^+((2)^2\Pi)$ is established. In the second case, our β parameters provide information on the symmetry of the superexcited intermediate states HCl^{**} [$\approx$70% of $^1\Sigma^+$ and $\approx$30% of $^1\Pi(1)$]. This fact leads to the revision of the results of the modeling of this channel in the recent study of Manzhos *et al.*[27] The repulsive $^1\Sigma^+(\sigma^2,\pi^3[(2)^2\Pi]4p\sigma)$ state is proposed to be the superexcited "gateway state" for the production of H^+ ions. The previously proposed bound $^1\Sigma^+$ is unlikely to be significant because of the spin-orbit state distribution of $\mathrm{Cl}(^2P)$.

Analysis of the Cl^+ ion production by REMPI $(2+1_i)$ and $(2+1_i+1)$ led to the conclusion that the fragmentation proceeds almost exclusively via repulsive Rydberg states of HCl^{**}. The largest contribution to each of the three main channels $\mathrm{H}+\mathrm{Cl}^*(4s)$, $\mathrm{H}+\mathrm{Cl}^*(4p)$, and $\mathrm{H}+\mathrm{Cl}^*(3d')$ comes from the photoexcitation of repulsive triplet states of HCl^{**} with a $^4\Pi$ core. These singlet-triplet transitions from $\mathrm{HCl}^*(B\,^1\Sigma^+)$ to HCl^{**} are likely due to the impurity of the $b\,^3\Pi_0$ state to the B state due to spin-orbit interaction. This assumption explains well the positive β parameters which were observed in all these cases experimentally. Fine structure distributions of Cl^* and markedly different spatial distributions for the individual channels agree very well with the proposed mechanism. However, where available, $^1\Sigma$ and $^1\Pi$ states of HCl^{**} may play a significant role in producing either $\mathrm{Cl}^*(4p)$, $\mathrm{Cl}^*(4s')$, or $\mathrm{Cl}^*(3d')$. A contribution of the REMPI $(2+1_i+1)$ channel in producing fast Cl^+ ions at $E_t \approx 2$ eV can also not be excluded.

This investigation has shown that the 3D mass-resolved REMPI is a powerful tool to study many-photon processes. It is hoped that the experimental results reported in this work will provide a stimulus for future theoretical analysis of such processes.

ACKNOWLEDGMENTS

The authors thank O. S. Vasyutinskii for helpful discussions. One of the authors (A.I.C.) gratefully thanks the support of the Alexander von Humboldt Foundation. Support by the Deutsche Forschungsgemeinschaft is gratefully acknowledged.

APPENDIX: DETERMINATION OF SPEED DISTRIBUTION FROM TOF PROFILES

In this Appendix we present a simple solution of the problem on how to restore the speed distribution of ions from TOF profiles. We assume isotropic angular distribution ($\beta=0$). The determination of the β parameter is the second problem which is simpler, and we shall not discuss it here. Such isotropic distributions may be constructed as $f(t) = n_\perp f_\parallel(t) + 2n_\parallel f_\perp(t)$, here $f_\parallel(t)$ and $f_\perp(t)$ are distributions obtained in experiments with polarizations $E \parallel Z$ and $E \perp Z$, respectively; $n_\parallel$ and $n_\perp$ denote the number of points in these distributions, respectively. The center of the distribution ($t=0$) is assumed to be known. For simplicity, we shall study symmetric functions $F(t)=(f(t)+f(-t))/2$ assuming $t>0$.

Ideally, the speed distribution $S(t)$ may be found as

$$S(t) = -\frac{d}{dt}F(t), \tag{A1}$$

dimensionless units t are assumed. Direct usage of this relation is impossible since the function $S(t)$ must be positive, while the experimentally determined $F(t)$ may fluctuate because of noise and some other specific reasons. Nevertheless, the best solution exists, and we denote it as $S(t)$. Using (A1), from $S(t)$ we can construct a TOF profile $\tilde{F}(t)$ as follows:

$$\tilde{F}(t) = \int_0^t S(\tau)\,d\tau. \tag{A2}$$

The difference between the original function $F(t)$ and the constructed $\tilde{F}(t)$ must be minimal. This is our criterium for the best $S(t)$ function. That is, we need to minimize the integral

$$J \equiv \int_t [\tilde{F}(t) - F(t)]^2 dt. \tag{A3}$$

Since $S(t)$ is not a smooth function, we need to formulate the problem in another language. Instead of the functions $F(t)$, $S(t)$, and $\tilde{F}(t)$ we use arrays F_i, S_i, and $\tilde{F}_i$, where i is an integer number, $1 \leqslant i \leqslant N$, usually $N \gg 1$. Equations (A1) and (A2) will be used in the following form:

$$\tilde{F}_i = \begin{cases} A & \text{if } i \leqslant K \\ 0 & \text{if } i > K \end{cases} \leftrightarrow S_i = \begin{cases} KA & \text{if } i = K \\ 0 & \text{if } i \neq K. \end{cases} \tag{A4}$$

That is, the derivative of a rectangular function is a δ function. As follows from Eq. (A4), the array $\tilde{F}_i$ constructed from an arbitrary array S_i must be nonincreasing, $\tilde{F}_{i+1} \leqslant \tilde{F}_i$; on the other hand, each nonincreasing array $\tilde{F}_i$ produces array S_i. Finding the best S_i means construction of a nonincreasing array $\tilde{F}_i$ for which the sum J is minimal,

$$J \equiv \sum_i [F_i - \tilde{F}_i]^2. \tag{A5}$$

We begin to construct the $\tilde{F}_i$ array starting from $i=1$ by using $\tilde{F}_1 = F_1$. Let us imagine that the first K elements of F_i obey the rule $F_{i+1} \leqslant F_i$, and hence the minimum of first K terms in J is achieved simply by using $\tilde{F}_i = F_i$, where $i \leqslant K$. Then we meet a local maximum in array F_i, the element which does not obey the rule, that is, $F_{K+1} > F_K$. Then we must change the value for $\tilde{F}_K$, and now a minimum of J is achieved at $\tilde{F}_K = \tilde{F}_{K+1} = (F_K + F_{K+1})/2$. Now the array $\tilde{F}_i$ may already be nonincreasing in the range $i \leqslant K+1$, but it may be that now $\tilde{F}_{K-1} < \tilde{F}_K$. In this case the value for J may be decreased again if we put $\tilde{F}_{K-1} = \tilde{F}_K = \tilde{F}_{K+1} = (F_{K-1} + F_K + F_{K+1})/3$.

If now the array $\tilde{F}_i$ is nonincreasing, we can continue to construct F_i from the point $i=K+2$. But if the array $\tilde{F}_i$ is still not nonincreasing, we must change the last four elements of $\tilde{F}_i$ $(K-2 \leqslant i \leqslant K+1)$, making them equal to the average of the last four elements of F. It is easy to show that this procedure again decreases the value for J. That is, the maximum "melts," and the "liquid" always flows in the direction $i=1$. Finally, we determine the nonincreasing array $\tilde{F}_i$ in the range $i \leqslant K+1$, and then we can continue to construct F_i from the point $i=K+2$.

This method is very easy to realize and, what is important, it provides an exact solution within the criterium (A3). In many cases some additional factors must be taken into account, such as the apparatus function, the limited size of the detector, and so on, then a forward convolution analysis must be used.[42] Even in these cases the present approach may be useful as a first approximation.

[1] P. Natalis, P. Pennetreau, L. Longton, and J. E. Collin, Chem. Phys. **73**, 191 (1982).

[2] T. A. Carlson, M. O. Krause, A. Fahlman, P. R. Keller, J. W. Taylor, T. Whitley, and F. A. Grimm, J. Chem. Phys. **79**, 2157 (1983).

[3] S. Svensson, L. Karlsson, P. Baltzer, B. Wannberg, U. Gelius, and M. Y.

Adam, J. Chem. Phys. **89**, 7193 (1988).
[4] H. Frohlich, P. M. Guyon, and M. Glass-Maujean, J. Chem. Phys. **94**, 1102 (1991).
[5] K. S. Haber, Y. Jiang, G. Bryant, and E. R. Grant, Phys. Rev. A **44**, R5331 (1991).
[6] R. G. Tonkyn, R. T. Wiedemann, and M. G. White, J. Chem. Phys. **96**, 3696 (1992).
[7] A. J. Yencha, A. J. Cormack, R. J. Donovan, A. Hopkirk, and G. C. King, Chem. Phys. **238**, 109 (1998).
[8] A. Yencha, G. King, M. Lopes, J. Bozek, and N. Berrah, Chem. Phys. Lett. **315**, 37 (1999).
[9] S. Arepalli, N. Presser, D. Robie, and R. J. Gordon, Chem. Phys. Lett. **118**, 88 (1985).
[10] R. Callaghan, S. Arepalli, and R. J. Gordon, J. Chem. Phys. **86**, 5273 (1987).
[11] T. A. Spiglanin, D. W. Chandler, and D. H. Parker, Chem. Phys. Lett. **137**, 414 (1987).
[12] E. de Beer, B. G. Koenders, M. P. Koopmans, and C. A. de Lange, J. Chem. Soc., Faraday Trans. **86**, 2035 (1990).
[13] D. S. Green, G. A. Bickel, and S. C. Wallace, J. Mol. Spectrosc. **150**, 354 (1991).
[14] D. S. Green, G. A. Bickel, and S. C. Wallace, J. Mol. Spectrosc. **150**, 388 (1991).
[15] D. S. Green, G. A. Bickel, and S. C. Wallace, J. Mol. Spectrosc. **150**, 303 (1991).
[16] Y. Xie, P. T. A. Reilly, S. Chilukuri, and R. J. Gordon, J. Chem. Phys. **95**, 854 (1991).
[17] D. S. Green and S. C. Wallace, J. Chem. Phys. **96**, 5857 (1992).
[18] A. Kvaran, A. Logadottir, and H. Wang, J. Chem. Phys. **109**, 5856 (1998).
[19] K. Wang and V. McKoy, J. Chem. Phys. **95**, 8718 (1991).
[20] E. de Beer, W. J. Buma, and C. A. de Lange, J. Chem. Phys. **99**, 3252 (1993).
[21] M. Penno, A. Holzwarth, and K.-M. Weitzel, Mol. Phys. **97**, 43 (1999).
[22] M. Michel, M. V. Korolkov, M. Malow, K. Brembs, and K.-M. Weitzel, Phys. Chem. Chem. Phys. **3**, 2253 (2001).
[23] A. Kvaran and H. Wang, Mol. Phys. **100**, 3513 (2002).
[24] D. M. Hurst and M. F. Guest, Mol. Phys. **41**, 1483 (1980).
[25] M. Bettendorff, S. D. Peyerimhoff, and R. J. Buenker, Chem. Phys. **66**, 261 (1982).
[26] C. Romanescu, S. Manzhos, D. Boldovsky, J. Clarke, and H.-P. Loock, J. Chem. Phys. **120**, 767 (2004).
[27] S. Manzhos, C. Romanescu, H.-P. Loock, and J. G. Underwood, J. Chem. Phys. **121**, 11802 (2004).
[28] A. I. Chichinin, T. Einfeld, K.-H. Gericke, and C. Maul, Chem. Phys. Lett. **390**, 50 (2004).
[29] S. Wolf and H. Helm, Phys. Rev. A **56**, R4385 (1997).
[30] S. Wolf and H. Helm, Phys. Rev. A **62**, R43408 (2000).
[31] D. H. Parker, R. F. Delmdahl, B. Bakker, and H. P. Loock, J. Chin. Chem. Soc. (Taipei) **48**, 327 (2001).
[32] A. Chichinin, T. Einfeld, C. Maul, and K.-H. Gericke, Rev. Sci. Instrum. **73**, 1856 (2002).
[33] A. Chichinin, K.-H. Gericke, T. S. Einfeld, and C. Maul, *Imaging in Molecular Dynamics: Technology and Applications* (University Press, Cambridge, 2003), p. 138.
[34] T. Einfeld, A. Chichinin, C. Maul, and K.-H. Gericke, J. Chem. Phys. **116**, 2803 (2002).
[35] T. Einfeld, A. Chichinin, C. Maul, and K.-H. Gericke, J. Chem. Phys. **117**, 1123 (2002).
[36] T. Einfeld, C. Maul, K.-H. Gericke, and A. Chichinin, J. Chem. Phys. **117**, 4214 (2002).
[37] M. Lampton, O. Siegmund, and R. Raffanti, Rev. Sci. Instrum. **58**, 2298 (1987).
[38] S. E. Sobottka and M. B. Williams, IEEE Trans. Nucl. Sci. **35**, 348 (1988).
[39] O. Jagutzki, V. Mergel, K. Ullmann-Pfleger, L. Spielberger, U. Meyer, and H. Schmidt-Bocking, Proc. SPIE **3438**, 322 (1998).
[40] M. Brown, M. Beckert, and U. Muller, Rev. Sci. Instrum. **71**, 4535 (2000).
[41] M. Drescher, A. Brockhinke, N. Böwering, U. Heinzmann, and H. Lefebvre-Brion, J. Chem. Phys. **99**, 2300 (1993).
[42] C. Maul, Phys. Chem. News **21**, 73 (2005).
[43] A. Eppink, S.-M. Wu, and B. Whitaker, *Imaging in Molecular Dynamics: Technology and Applications* (University Press, Cambridge, 2003), p. 65.
[44] A. D. Pradhan, K. P. Kirby, and A. Dalgarno, J. Chem. Phys. **95**, 9009 (1991).
[45] D. S. Ginter and M. L. Ginter, J. Mol. Spectrosc. **90**, 177 (1981).
[46] L. Singleton and P. Brint, J. Chem. Soc., Faraday Trans. **93**, 21 (1997).
[47] J. B. Nee, M. Suto, and L. C. Lee, J. Chem. Phys. **85**, 719 (1986).
[48] K. Gödderz, N. Schwentner, and M. Chergui, Chem. Phys. **209**, 91 (1996).
[49] NIST Standard Reference Database 78, NIST Atomic Spectra Database, http://physics.nist.gov/PhysRefData/ASD/index.html
[50] H. Frohlich and M. Glass-Maujean, Phys. Rev. A **42**, 1396 (1990).
[51] H. Wang and A. Kvaran, J. Mol. Struct. **563**, 235 (2001).
[52] A. D. Pradhan, K. P. Kirby, and A. Dalgarno, J. Chem. Phys. **103**, 864 (1995).
[53] R. Liyanage, R. Gordon, and R. Field, J. Chem. Phys. **109**, 8374 (1998).
[54] J. B. Nee, J. Phys. B **23**, 3325 (1990).
[55] M. Heninger, S. Fenistein, G. Mauclaire, R. Marx, and Y. M. Yang, J. Chem. Soc., Faraday Trans. 2 **85**, 1705 (1989).
[56] M. V. Korolkov, K.-M. Weitzel, and S. D. Peyerimhoff, Int. J. Mass. Spectrom. **201**, 109 (2000).
[57] H. Lefebre-Brion, P. M. Dehmer, and W. A. Chupka, J. Chem. Phys. **88**, 811 (1988).
[58] T. A. Carlson, G. E. McGuire, A. E. Jonas, K. L. Cheng, C. P. Anderson, C. C. Lu, and B. P. Pullen, *Electron Spectroscopy* (North Holland, Amsterdam, 1972).
[59] P. K. Ghosh, in *Introduction to Photoelectron Spectroscopy*, Chemical Analysis, Vol. 67 (Wiley, New York, 1983).
[60] J. W. Rabalais, *Principles of Ultraviolet Photoelectron Spectroscopy* (Wiley, New York, 1977).
[61] J. H. D. Eland, *Photoelectron Spectroscopy* (Butterworths, London, 1974).
[62] K. L. Reid, D. L. Leahy, and R. N. Zare, J. Chem. Phys. **95**, 1746 (1991).
[63] H.-P. Loock (private communication).
[64] M. Michel, M. V. Korolkov, and K.-M. Weitzel, Phys. Chem. Chem. Phys. **4**, 4083 (2002).
[65] A. A. Radzig and B. M. Smirnov, in *Reference Data on Atoms, Molecules, and Iones*, Chemical Physics Vol. 31 (Springer-Verlag, Berlin, Heidelberg, 1985).
[66] V. Aquilanti, D. Ascenzi, M. de Castro Vitores, F. Pirani, and D. Cappelletti, J. Chem. Phys. **111**, 2620 (1999).
[67] F. Pirani, D. Cappelletti, M. Bartolomei, V. Aquilanti, M. Scotoni, M. Vescovi, D. Ascenzi, and D. Bassi, Phys. Rev. Lett. **86**, 5035 (2001).
[68] M. Alexander, X. Li, R. Liyanage, and R. Gordon, Chem. Phys. Lett. **231**, 331 (1998).